Scattering of 64.3-MeV Alpha Particles from Nickel-58 and Iron-58†

P. DARRIULAT,* G. IGO, H. G. PUGH, J. M. MERIWETHER, AND S. YAMABE‡
Lawrence Radiation Laboratory, University of California, Berkeley, California
(Received 18 November 1963)

For 64.3-MeV α particles the differential cross sections for elastic scattering and excitation of the first 2^+ collective state have been measured for the Ni^{58} and Fe^{58} isobars at approximately 0.5° intervals between 10° and 82° in the center-of-mass system. The measurements were made with sufficient precision to follow the rapid variations and deep minima in the angular distributions, and the data have been exhaustively studied for possible errors; an extensive discussion of the uncertainties is given. An analyzed beam (energy spread <100 keV) of high-energy alpha particles was afforded by the Berkeley 88-in. sector-focused cyclotron. The analyzed beam was characterized by high intensity (0.5 μA), small angular divergence (<0.17°), small beam width (0.06 in.), and by small energy variation during the experiment (±100 keV). A precise scattering chamber (typical tolerance <0.01°) and solid-state detectors with small angular acceptance (0.5°) and sufficient energy resolution (150 keV) were used. No attempt has been made to fit the angular distributions in detail but approximate fits to the elastic scattering obtained using an optical potential show: (a) It is not possible to account for the differences observed between the elastic scattering cross sections for the two isobars merely in terms of their different charge or charge distribution. (b) At large angles the elastic scattering from Fe^{58}, about half as intense as from Ni^{58}, can be qualitatively described by using a deeper absorptive potential for Fe^{58}. Analysis of the elastic- and inelastic-scattering cross sections for $\theta_{c.m.}<50°$ using the smooth cutoff model of Blair, Sharp, and Wilets gives the quadrupole deformation parameter β as 0.15 (Ni^{58}) and 0.17 (Fe^{58}).

A. INTRODUCTION

THE optical model of the nucleus, becoming more and more elaborated, attempts to account for more and more detailed properties of nuclei. More, and more accurate, experimental data are therefore required.

We have studied, using a high-precision scattering chamber and solid-state detectors, the scattering of 64.3-MeV α particles from the Ni^{58} and Fe^{58} isobars. We have tried to obtain as accurately as possible the differential cross section for elastic scattering and for inelastic excitation of the first 2^+ state over an angular range between 10° and 80°.

Two main reasons led us to this choice of experiment:

(a) Interest has recently been shown in the possibility of explaining the proton anomaly[1] already observed and investigated for several years, by adding to the classical optical potential a term $V_T\mathbf{t}\cdot\mathbf{T}$ depending on the isotopic spins $\mathbf{t}$ and $\mathbf{T}$ of the incident particle and target nucleus.[2–4] Fulmer,[5] at 22 MeV, and more recently Benveniste *et al.*,[6–10] at 10.9 and 11.7 MeV, investigated for that purpose proton scattering from Ni^{58}, Fe^{58} and other pairs of isobars. The differences they observed were, however, so small that the interpretation of their results, especially at 22 MeV, was not easy. It was therefore of interest to investigate to what extent it is permissible to assign the responsibility for *all* the differences observed to the isotopic-spin-dependent potential. Alpha-particle scattering seemed an appropriate tool for this investigation since there can be no isotopic-spin term involved and in addition it is sensitive to the external part of the nucleus, a region where two isobars are most likely to differ.

(b) On the other hand, calculations recently performed on the scattering of 43-MeV α particles from Ni^{58} and Ni^{60} by Bassel *et al.*[11,12] (distorted-wave Born approximation), Buck[13] (coupled wave equations), and by Blair *et al.*[14] (smooth cutoff model) were able to describe successfully the experimental cross sections[15,16] for the ground states and for the excited states of these nuclei. It was therefore hoped that any differences observed between Ni^{58} and Fe^{58} could be expressed meaningfully in terms of differences between the parameters of these models and give a better understanding of the structure of these nuclei.

B. EXPERIMENTAL ARRANGEMENT

B1. Beam Optics

The layout of the 88-in. cyclotron and experimental area is shown in Fig. 1. A beam of α particles is extracted

† Work done under the auspices of the U. S. Atomic Energy Commission.
* N.A.T.O. Fellow (1962–1964), on leave from C.E.N. Saclay.
‡ On leave from Osaka University, Osaka, Japan.
[1] A. E. S. Green and P. C. Sood, Phys. Rev. **111**, 1147 (1958).
[2] J. D. Anderson, C. Wong, and J. W. McClure, Phys. Rev. **126**, 2170 (1962).
[3] A. M. Lane, Phys. Rev. Letters **8**, 171 (1962).
[4] F. Perey, Phys. Rev. **131**, 745 (1963).
[5] C. B. Fulmer, Phys. Rev. **125**, 631 (1962).
[6] J. Benveniste, R. Booth, and A. C. Mitchell, Phys. Rev. **123**, 1818 (1961).
[7] J. Benveniste, A. C. Mitchell, and C. B. Fulmer, Phys. Rev. **129**, 2173 (1963).
[8] J. Benveniste, A. C. Mitchell, and C. B. Fulmer, Phys. Rev. **130**, 309 (1963).
[9] J. Benveniste, A. C. Mitchell, and C. B. Fulmer, Phys. Rev. **133**, B317 (1964).
[10] J. Benveniste, A. C. Mitchell, B. Buck, and C. B. Fulmer, Phys. Rev. **133**, B323 (1964).
[11] R. H. Bassel, G. R. Satchler, R. M. Drisko, and E. Rost, Phys. Rev. **128**, 2693 (1962).
[12] E. Rost, Phys. Rev. **128**, 2708 (1962).
[13] B. Buck, Phys. Rev. **127**, 940 (1962).
[14] J. S. Blair, D. Sharp, and L. Wilets, Phys. Rev. **125**, 1625 (1962).
[15] R. Beurtey, P. Catillon, R. Chaminade, M. Crut, H. Faraggi, A. Papineau, J. Saudinos, and J. Thirion, J. Phys. Radium **21**, 399 (1960).
[16] H. W. Broek, T. H. Braid, J. L. Yntema, and B. Zeidman, Phys. Rev. **126**, 1514 (1962).

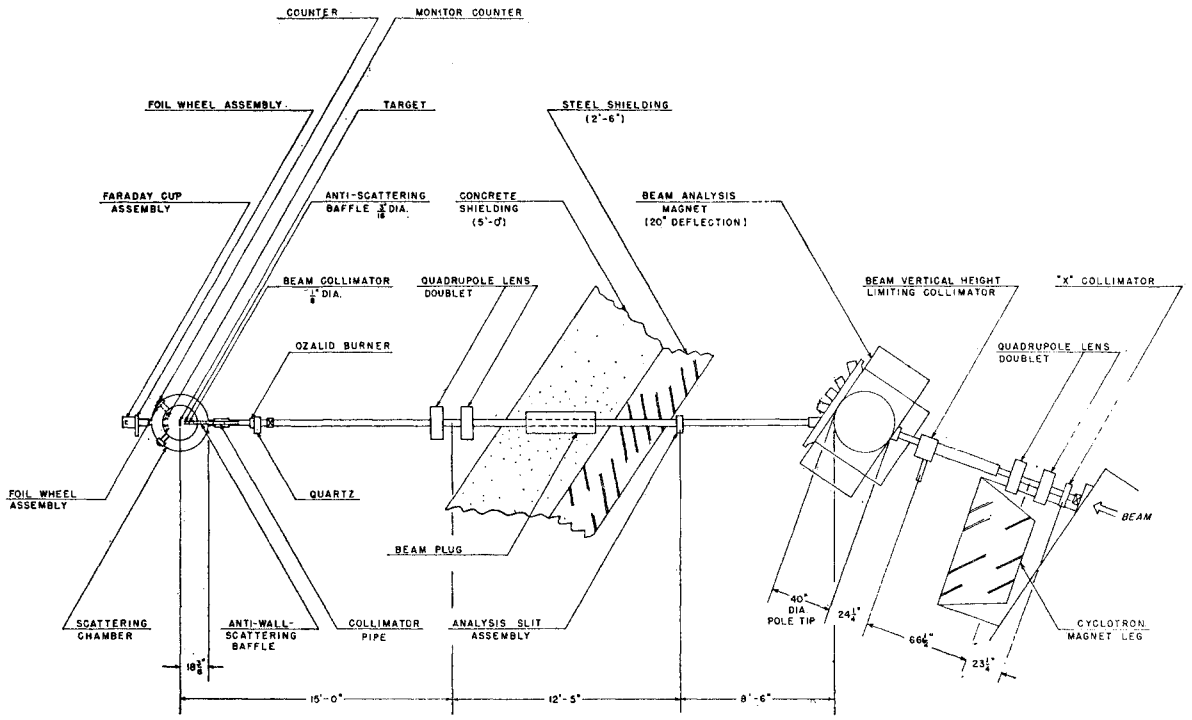

FIG. 1. The experimental layout.

by means of an electrostatic deflector; after passing through the fringe field of the main magnet it appears as if radiating from a virtual source 0.45 in. high and 0.15 in. wide with a total angular divergence of 0.0088 rad vertically and 0.034 rad horizontally. The total momentum spread of the beam is $\Delta p/p = 0.004$.

Figure 2 shows typical beam particle trajectories in the horizontal and vertical planes. A remotely controlled, adjustable, vertical slit (X collimator) was used to limit the angular divergence in the horizontal plane before the beam entered the first quadrupole doublet. The beam then passed through a horizontal slit 0.5 in. high which limited the angular divergence in the vertical plane and a magnet which deflected the beam 20° to the west; an image of the virtual source was produced 20 ft downstream from the first quadrupole doublet. At this focus an adjustable slit permitted a momentum analysis of the beam. For a 0.1-in.-wide analyzing slit the energy spread in the beam was calculated to be 100 keV.

A second quadrupole doublet produced an image of the analyzing slit in the center of the scattering chamber. This image was about 0.06 in. wide and 0.06 in. high and the beam at this point had a vertical angular divergence of ± 0.0007 rad while its horizontal angular divergence, determined by the X collimator setting, was ± 0.0014 rad or ± 0.0029 rad in different parts of the experiment.

The beam intensity was varied between 2 mμA and 500 mμA by adjustments of the X collimator, analyzing slit, and the circulating beam intensity.

The beam energy was 64.5 ± 1 MeV calculated from the dee frequency of the cyclotron which was 8.97 ± 0.01 Mc/sec. The dependence of the external beam energy on dee frequency was determined in separate experiments from range-energy measurements. The pulse height in the monitor counters remained constant within ± 100 keV throughout the experiment except in two cases: When the X collimator was opened, the mean energy dropped by 100 ± 100 keV and for a small part of the time the energy was 200 ± 100 keV low because the dee frequency was misset.

B2. Scattering Chamber

In this section the basic features of the Berkeley 17-in. scattering chamber are described; additional equipment added for this experiment is described in Sec. B4.

A vertical section of the scattering chamber and associated equipment is shown in Fig. 3. The chamber consists of a fixed center plate A of internal radius $9\frac{3}{4}$ in. and external radius 17 in. separated from a base plate B by three pillars (not shown) separated by 120°. Two rotatable turrets C and D are located relative to the center plate by means of the ball races E. Each turret has four precision ground flats F and bores G spaced at intervals of 90°. These define axes passing

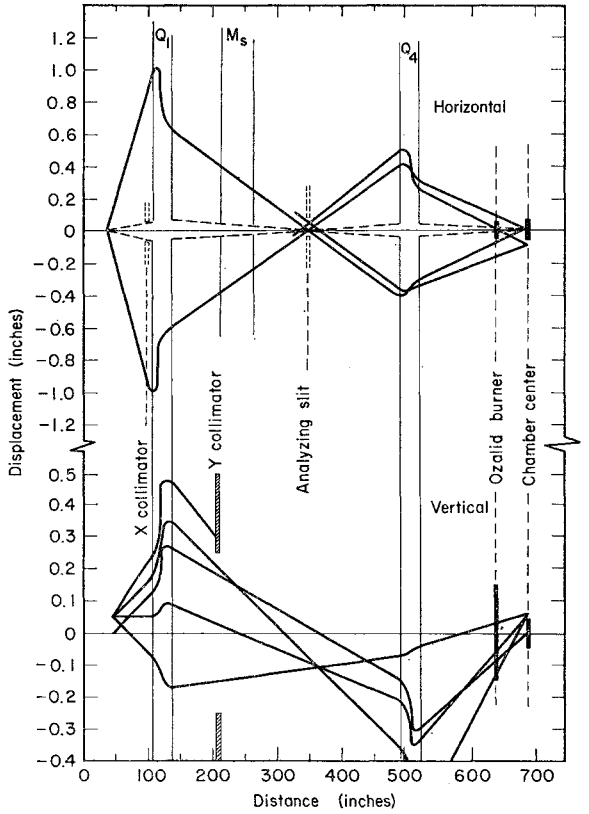

FIG. 2. Typical beam particle trajectories in the horizontal and vertical planes. In the horizontal plane two configurations are shown: (a) with the X collimator open and the analyzing slit set at 0.10 in. (solid lines) and (b) with the X collimator and the analyzing slit closed down (dashed lines). The distances along the beam lines denoted Q_1, Ms, and Q_4 are the positions and effective lengths of the first quadrupole, the bending magnet, and the second quadrupole, respectively. The X collimator, Y collimator, analyzing slit, and ozalid burner are described in Sec. B1. The heavy black lines at the ozalid burner position and chamber-center position show the vertical and horizontal profile of the beam. The intense core of the beam is smaller, approximately 0.06 in. in diameter.

through the center of the chamber at angles 10° above and below the median plane so that scattering angles from 10° to 170° may be studied. In the figure the counter assemblies are shown at a scattering angle of $\theta=10°$; if the turrets are rotated through θ_H the new scattering angle is given by $\cos\theta=\cos\theta_H \cos 10°$.

The base plate B is supported on a stand which has three planer jacks for height adjustment and leveling. The stand also provides for adjustment of the chamber horizontally at right angles to the beam direction and allows rotation of the chamber about a vertical axis passing through its center.

The target frame H, which holds four targets, can be rotated and adjusted in height. The targets can be raised into the glass cylinder J for inspection and for protection while the chamber is let down to air. When burns are made on photosensitive "ozalid" paper in the target position to find the beam position, these can be viewed through Mylar windows in the center plate without moving the target.

An internal Faraday cup K with electrostatic guard ring L can be raised into the beam.

The vacuum seals are made by lightly greased polyethylene rings M and the vacuum is maintained at about 5×10^{-5} mm Hg by a 4-in.-diam oil diffusion pump with a liquid nitrogen vapor trap.

The angles are read directly on vernier scales which enable them to be set at 0.1° intervals with an accuracy of ±0.005°. The target height and Faraday cup height are read on linear scales.

All movements are controlled by motor drives which can be operated remotely.

B3. Precision of the Scattering Chamber

In the design and construction of the scattering chamber considerable care had been taken to insure accuracy in the principal movements and dimensions. Typical tolerances are ±0.001 in. for the distance of the precision flats F from the center and ±0.005° in the graduated scales.

We used a telescope to make a number of tests on the accuracy of construction, usually with a precision of about 0.01°. The precision flats F and bores G were used as the basis of the test and a telescope mount was constructed to fit them; in addition, a sighting object was made to fit the target frame.

With a sighting object in the target frame and the telescope on the upper turret it was found by separate rotation of the turret and target that the axis of rotation of the target differed from that of the turret by 0.002±0.001 in.

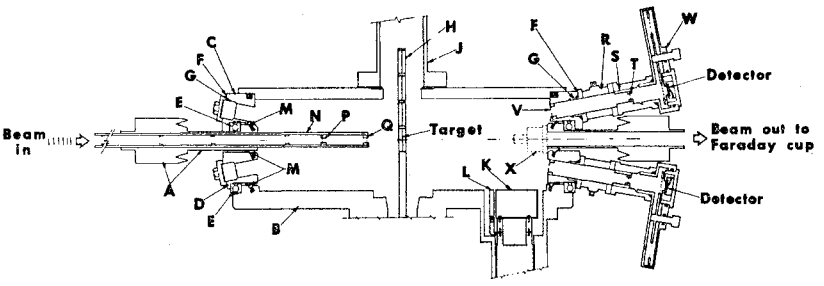

FIG. 3. Schematic diagram of the scattering chamber and associated equipment. The lettered quantities are discussed in Sec. B2.

With a sighting object on the lower turret and the telescope on the upper turret it was found that the distance between the planes of rotation of the upper and lower turrets was 0.001 ± 0.002 in. greater than specified while the axis of rotation of the two turrets were parallel to an accuracy of $\pm0.01°$. When the chamber was pumped out, measurements with a dial indicator showed that the separation of the upper and lower turrets decreased by 0.0021 ± 0.0006 in.

B4. Additional Equipment Associated with the Scattering Chamber

The beam entered the chamber through a collimator pipe N mounted on the fixed center plate of the chamber (see Fig. 3). Circular baffles located in the pipe served to prevent wall scattering and a $\frac{3}{32}$-in.-diam aperture P cleaned up the edges of the beam. This aperture, like all the other collimators used in the experiment, was made of tantalum sheet 0.020 in. thick, a little more than the range of 65-MeV α particles. The aperture Q of $\frac{1}{8}$-in.-diam served as an antiscattering baffle. The beam, after passing through the target, entered a Faraday cup outside the chamber (not shown in Fig. 3) protected against charge loss and gain by a permanent magnet; this Faraday cup was used rather than the internal one, except for tests, because of the large background counting rates produced by the beam striking the internal Faraday cup.

Four lithium-drifted silicon detectors (see Sec. B6) were used, one mounted on each of the two turrets and two mounted on the center plate as monitors of the product of beam intensity times target thickness and of the beam position (see Sec. D4). The assembly for each movable counter consisted of a ball valve R and collimator pipe S which were aligned mechanically with respect to the precision flat F and bore G. The collimators T, 16.37 in. from the target, were rectangles approximately 0.170 in.$\times$0.065 in. formed from four pieces of tantalum whose edges were ground flat to an accuracy of 0.0001 in. The solid angles were thus about 5×10^{-5} sr, and taking into account the characteristics of the beam the angular resolution was about 0.5°. A detailed account of the consequences of the chamber geometry including angular resolution and effects of beam misalignment is given in Appendices II and III. One consequence of the chamber geometry is that at $\theta_H=0$ ($\theta=10°$) the counter collimator contributes to the angular resolution function solely through its vertical height whereas at large angles the usual situation prevails where only the horizontal width is important; therefore at small angles we set each collimator so that its larger dimension was horizontal while for angles greater than $\theta_H=10°$ ($\theta=14°$) we rotated it through 90° so that the larger dimension was vertical. The antiscattering baffles V prevented the counters from seeing any of the baffles in the beam line. Each of the movable counters was preceded by a foil wheel assembly W used for testing purposes which also carried an Am^{241} α-particle source for preliminary adjustments of the electronics.

The two monitor counters X were supported on the inside of the center plate by permanent magnets; no provision was made for accurate positioning. The collimators for these were $\frac{1}{16}$ in. in diameter at $8\frac{1}{2}$ in. from the target, giving approximately the same angular resolution as for the movable counters.

The counter angles, target angle, and height were all set by remote control from the counting area and the scales were read via television cameras. It was not realized until late in the run that because of poor definition of the image and parallax effects the use of television caused a considerable sacrifice of accuracy. The angular uncertainty introduced was about $\pm0.05°$ and is the major uncertainty in much of our data.

B5. Alignment of the Scattering Chamber

The scattering chamber was centered on the beam line by the following procedure. Ozalid burns were made at both ends of the collimator pipe with the Ta baffles and beam collimator removed (see Fig. 3). The chamber was adjusted until the collimator pipe was centered on the ozalid burns. An ozalid burn at the target then showed the beam was 0.032 in.$\pm$0.016 in. west and 0.032 in.$\pm$0.016 in. high since the beam collimator tube was slightly misaligned with respect to the center of the chamber. The detector angular setting correction and solid-angle correction which arose were small so that first-order corrections to these two quantities sufficed. These corrections are discussed in Appendix II.

B6. Counters

The counters, which were 0.8 in. in diameter and 0.08 in. thick were lithium-drifted silicon detectors made by a procedure described in Ref. 17. In order to reduce window effects, the entrance face was lapped and etched and a surface barrier was formed. Silicone varnish was painted around the edge of the surface barrier forming a raised rim and gold was evaporated over the whole entry face including the rim. In the counter assembly (Fig. 4) contact to the "mesa" was

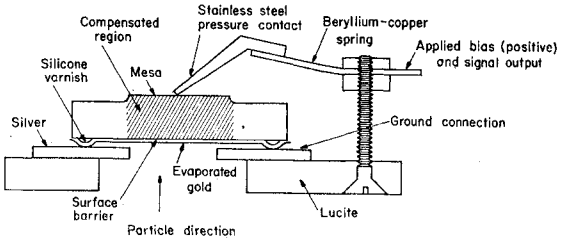

FIG. 4. Schematic diagram of the detector and of the detector assembly.

[17] J. H. Elliott, Nucl. Instr. Methods 12, 60 (1961).

made by a stainless-steel pressure contact which also pressed the raised rim on the entry face against a silver sheet to provide contact to the surface barrier. This method of construction and assembly made handling of the detectors convenient and safe.

The bias voltages applied were between 200 and 600 V, depending on the detector; and the leakage currents were 1.5 to 6 μA.

B7. Electronics

Four counters were used, two of them movable and two used as fixed monitors. Each counter was connected by a short length of low-capacity cable to the input of an LRL Mod VI preamplifier[18] and via a 100-kΩ resistor to the bias supply. The preamplifier output signals had a rise time of 200–300 nsec and a decay time of 35 μsec. They traveled to the counting area through a long length of 125-Ω cable terminated at the input of an LRL Mod VI main amplifier.[18] In the main amplifier the pulses were differentiated with a time constant of 2.5 μsec, amplified, and then passed through a shaping circuit with rise time and fall time of 1 and 2.5 μsec, respectively. A biased output enabled us to select the upper part only of the energy spectrum for display and analysis.

The spectra from all four counters were mixed and fed into the common amplitude-to-digital converter of a 400-channel pulse-height analyzer. Small fractions of each pulse split off before the mixer and used to fire a discriminator and scaler and a single-channel pulse-height analyzer. The output of a single channel was used to determine in which of the four 100-channel segments of the analyzer the pulse from the mixer should be recorded. Thus the analyzer stored the spectra from both movable counters and both monitors. All dead-time losses applied equally to all the spectra and corrections for dead time did not have to be applied in calculating relative cross sections. Coincidence and anti-coincidence circuits were used to insure that the analyzer could not receive any pulse unaccompanied by a routing pulse, any pulse accompanied by a routing pulse to the wrong quadrant, or two pulses simultaneously. The system was checked using test pulses and also under approximate running conditions by disconnecting the bias supply from each counter in turn and showing that no pulses arrived in the corresponding quadrant of the analyzer. In order to insure small dead-time corrections, small pileup of pulses, and correct operation of the routing system, the counting rate in each quadrant of the analyzer was kept below 100 per sec.

The gains were set up to give a channel width of about 100 keV per channel with the upper 8 MeV of each spectrum displayed. Because of the threshold circuits the response was nonlinear, the effect being most serious in the low channels. The energy calibration was obtained by feeding test pulses directly into the detectors from a linear pulse generator and by comparison with inelastic scattering to known excited states of carbon.

The control system for the counting equipment was operated from the live-time integrator of the pulse-height analyzer. A preset value for the live time was chosen, usually 20 min. At the end of this period, the analyzer stopped and a pulse was generated which stopped all the scalers and the beam integrating system. The scalers recorded the number of counts from each counter up to an excitation of about 5 MeV, the clock time as determined from the line frequency and from a 1000-cps crystal-controlled oscillator, and the number of "dumps" of the current integrating system (the fractional part of the last "dump" was read from the pen-recorder). The scalers on each counter were not used directly in the analysis but served in several instances to show that the data had been incorrectly recorded (for example, if the pulse-height analyzer was not cleared at the beginning of a run).

After each run the four spectra on the pulse-height analyzer were printed out, transferred via magnetic tape to a "slave" analyzer, and plotted out (a relatively slow procedure) while the "master" analyzer was freed to take new data.

C. EXPERIMENTAL PROCEDURE

C1. Tests

A series of tests are described which were made prior to and during the data-taking runs.

(a) The monitor counters were fixed at approximately $\pm 15°$ relative to the beam direction, and with the movable counters at various angles, tests were made to show that target-out backgrounds were negligible.

(b) A thin gold-leaf target was inserted. By studying the counting rates in the movable counters near the zeros of their scale angles it was shown that the scale zeros agreed within 0.03°.

(c) Nickel-58 and iron-58 targets of thickness approximately 6.3 mg/cm^2 were inserted in the target frame. For each target the sum of the monitor yields normalized to the integrated beam current was studied as a function of the height of the target relative to the beam. This gave a measure of the homogeneity of the target along the vertical axis, averaged over the size of the beam spot. The most uniform part of each target was selected. Throughout the experiment the targets were always replaced at the same height to an accuracy of ± 0.005 in. It was found that this uncertainty caused fluctuations in the monitor yield of the order of $\pm 2\%$ whereas for pairs of measurements between which the target was not moved the monitor yield was constant within the statistical uncertainty. This information was useful towards the end of the run, when one of the monitor counters failed, as a $\pm 2\%$ check on the remaining counter.

[18] W. W. Goldsworthy, Lawrence Radiation Laboratory Report UCRL-9816, 1961 (unpublished).

(d) The internal and external Faraday cups were compared using the monitor yield for normalization. The voltage on the guard ring of the internal Faraday cup was increased until a plateau was reached. It was found that the current recorded by the internal Faraday cup was larger than that in the external Faraday cup by $(1.0\pm1.3)\%$. The uncertainty is large because the background produced by the internal Faraday cup made analysis of the monitor spectra difficult. A current source continuously monitored by a standard-cell potentiometer could be connected to the electrometer for calibration purposes. Tests were made which showed that the measured charge was not affected by stray capacities or leakage resistances in the Faraday cup and connection cables. The calibration was obtained to an accuracy of $\pm0.3\%$ for the beam intensity used in the absolute cross-section runs (see Sec. C3) before and after the measurements.

(e) The detectors were tested for linearity in two ways, the movable counters by elastic scattering from gold with aluminum degraders and the monitor counters (which had no foil wheels) by studying elastic and inelastic scattering from carbon. One of the monitors was found to be insufficiently thick, and a 0.003-in. thickness of aluminum foil had to be inserted in front of it; this had the effect of spoiling the energy resolution to some extent.

(f) The energy resolution of the detectors for scattering from a thin gold-leaf target was about 150 keV full width at half-height. This figure is approximate since it is little more than the channel width of the pulse-height analyzer. This resolution is mainly due to three factors of comparable importance: noise from the detector, noise from the preamplifier, and 60-cps noise from the main amplifier. The energy deteriorated as the counting rate was increased and simultaneously an asymmetry of the peak shape (more pronounced on the low-energy side) appeared. Further remarks on the peak shape will be found in Sec. D1 on the spectrum analysis. For most of the data runs, the energy resolution was between 200 and 400 keV.

(g) The relative efficiency of the detectors was tested in the following ways: Before the run began, each counter was tested with low-energy α particles from an Am^{241} source. The counting rate was measured as a function of the area of a collimator inserted in front of the detector. The counting rate was proportional to area up to sizes of collimator larger than those used in the experiment. A small fraction of pulses fell below the peak. This fraction depended on the collimator material and sharpness of edge. The lowest fraction measured was less than 1%. This test checks little more than the surface barrier region of the detector. As a second test both of the movable detectors were set up at a maximum for elastic scattering from Ni^{58} and several simultaneous spectra were recorded for the two detectors. Then the counter holders and preamplifiers were interchanged and several more pairs of spectra recorded. Finally the counters were returned to the original positions and a further measurement made. Taking ratios to eliminate the areas of the collimators, target thickness, and integrated beam intensity, two values of the relative efficiency were obtained. These were 1.000 ± 0.004 and 0.993 ± 0.004. The counters have therefore been assumed to be equally efficient. We have not, however, made any measurement of the absolute efficiency of the detectors. We assume it to be unity.

(h) Three angular sequences A, B, and C were used in taking data. Sequences A and B were designed to look for monitor failure, current integration failure, target deterioration, loss of energy resolution in the beam or in the detectors, and other sources of error which are time dependent. Sequence C was used only during the last part of the experiment ($\theta_{c.m.}>56°$).

In sequence A, angular measurements are made at 1.0-deg intervals by the top and bottom counters but staggered by 0.5 deg, proceeding from the minimum angle to the maximum angle of the range under consideration. Then the process is repeated in reverse order (i.e., from the maximum to the minimum angle) with the set of angles measured by top and bottom counters reversed. Thus each measurement is repeated twice—once by each counter.

In sequence B, the procedure is identical to A except that the angular measurements are made at 2.0-deg intervals by the top and bottom counters. Consequently, measurements are made at 0.5-deg intervals without repeats.

In sequence C, used only for a few runs, the angular measurements are made at 2-deg intervals by the top and bottom counters staggered by 1 deg, from the minimum angle to the maximum angle only.

(i) Measurements were made at each angle for both Ni^{58} and Fe^{58} changing only the target setting. Next the top and bottom counters were rotated to two new angles without moving the target position. The former part of the procedure eliminated to a great extent an uncertainty in the ratio of the cross sections since the ratio taken at a fixed angle is insensitive to the setting error. The latter part of the procedure made it possible to check on the constancy of the ratio of monitor counts to integrated beam from run to run.

(j) A limited analysis of the data for consistency checks during the experiment was possible. Runs of twenty minutes usually provided adequate statistical accuracy and gave a reasonable duty cycle since only five minutes were required to change angles or target position, read and mechanically plot out the data, and reset the equipment for the next run.

C2. Relative Cross-Section Measurements

The beam handling parameters were adjusted as follows for the measurements at small angles. The analyzing slit width was set at 0.020 in. and the X collimator to a nominal setting of 0.08 in. This gave a

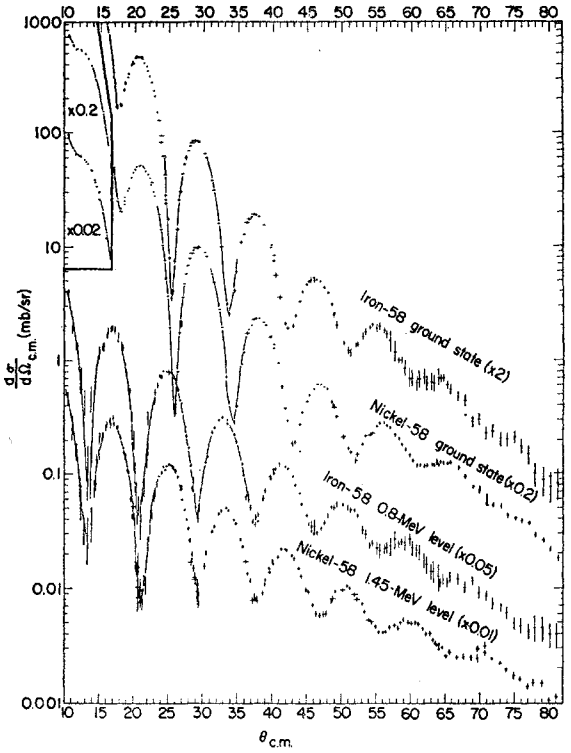

FIG. 5. The differential cross sections in the center-of-mass system for elastic scattering and excitation of the first excited (2+) states in Ni^{58} and Fe^{58}.

beam intensity of between 2 and 4 mμA. An ozalid burn was made at the target position; the beam spot was found to be 0.032 in.±0.016 in. low and 0.032 in. ±0.016 in. west, with a diameter of 0.060 in. The counter collimators were inserted in a horizontal position (i.e., 0.065 in. high and 0.170 in. wide) and relative cross-section measurements were begun at 0° scale ($\theta=10°$) following sequence *A*. The above measurements were made with both movable counters on the east (E) side of the beam line. Next, two angles were repeated for Ni^{58} with the counters on the west (W) side as a check on the beam direction.

Measurements were continued from $\theta=15.5°$ to 21.5° using sequence *A* with the counter collimator rotated (i.e., 0.170 in. high and 0.065 in. wide). One pair of angles was repeated after the collimators were rotated. The beam intensity was increased to 10–15 mμA by opening the *X* collimator to a nominal width of 0.10 in.

Measurements were made from $\theta=22°$ to 26.5° using sequence *A*, and from 27° to 37.5° using sequence *B*. The monitors were moved to 27°, approximately a maximum in the ground-state differential cross sections. The beam intensity, 100–150 mμA, was obtained by opening the analyzing slit to 0.10 in.

The next range of angles measured was from $\theta=35°$ to 45.5° using sequence *B*. The monitor counters were moved to another maximum of the ground state at ±43.5° (see Fig. 5) to reduce the dead time on the pulse-height analyzer. The relative normalization of the monitor data was next obtained (see Sec. D2 for details).

Four more pairs of points were obtained on part of a new cycle from $\theta=46°$ to 53.5° following sequence *B*. During these runs it was suspected that the beam position had changed. An ozalid burn at the target position showed the beam had moved $\frac{1}{8}$ in. E. Since the point at which this shift occurred is uncertain, the angular uncertainty for these data is correspondingly large (see Fig. 5).

For the remaining measurements the beam intensity was increased to 500 mμA by increasing the circulating beam. The collimator pipe, consequently, became overheated and simultaneously a film appeared on the inside of the chanber and on all exposed surfaces, evaporated from the collimator pipe. Some of the deposit wiped from the inside of the chamber was analyzed immediately for iron and nickel: the tests were negative. Deposits on the target surface were qualitatively analyzed at the end of the experiment. The predominant constituent was cadmium, with much smaller amounts of zinc and traces of chromium. Tests for Fe, Ni, Nb, Mn, Mo, Sn, V, Y, and Zr were negative. In the analysis of the spectra the cadmium ground state and first excited state were present in the Fe^{58} spectra and necessitated corrections of the order of 1%. No other contaminant peaks were observed. Zinc-excited states would have been visible if the contamination had been appreciable. No contaminants at all were visible in the Ni^{58} spectra. It is presumed that the contamination was projected in a jet down the collimator pipe at a time when the Fe^{58} target was under bombardment.

After reducing the beam appropriately, the measurements were continued from $\theta=54°$ to 60° using sequence *B*. At this point the energy resolution had deteriorated badly because of energy losses in the target. The target was therefore rotated by 18°, the angle being limited by geometry factors imposed by the shape of the target frame and the angles of the monitor counters. Because of obstruction by a supporting pillar in the chamber, it was also necessary for the movable counters to be operated on the west (W) side of the chamber. Tests were made to show that changing the target angle did not change the monitor-counter ratio.

Measurements were continued at 1.0° intervals out to $\theta=76°$, using sequence *C*. During this set of measurements one of the monitor counters became progressively worse and finally failed. At the end of the experiment an ozalid burn was made in the target position.

C3. Absolute Cross-Section Measurements

For these measurements (called the "*C*" runs) new targets were used, rolled from the same isotopic material as the targets for the relative cross-section measurements. Several points on the angular distribution near the ground-state maximum at $\theta=19.5°$ were measured

using the Faraday cup as a monitor and relative cross-section measurements described in Sec. C1 were normalized to these. The fitting procedure is described in Sec. D4.

A target holder was assembled containing the Fe^{58} and Ni^{58} targets and two ozalid papers. Using a beam of 25 mμA the uniformity of each target averaged over the size of the beam spot was measured along a vertical line and the target height for the most uniform region was noted.

The current integrating system was calibrated using a constant current source providing 25 mμA. An ozalid burn was taken at the target position. The measurements on the 19.5° maximun were made, each target being kept fixed at its predetermined height throughout, another ozalid burn was taken and finally the current integrator was recalibrated.

The positions of the ozalid papers relative to each other and to the target position were accurately known from the target height scale. The papers and targets were removed and compared; the two ozalid burns were identical. An ozalid paper was laid over each target and the target area corresponding to the size and position of the beam spot was cut out. These samples of the target were weighed using a balance sensitive to 0.001 mg and their areas were determined using a traveling microscope accurate to 1 μ. Each target sample was next cut into four pieces and the weight and area measurements were repeated. From the target homogeneity measurements made in the vertical direction using the beam and by comparison of the measurements of the whole and four pieces of the target samples the uncertainty in target mg/cm^2 was estimated to be $\pm 2.2\%$ for Ni^{58} and $\pm 2.7\%$ for Fe^{58}. Corrections of $(0.36\pm 0.05)\%$ and $(1.05\pm 0.06)\%$ were made to the target masses for the presence of contaminants (see Sec. D2).

The uncertainty on the integrated beam current was taken as $\pm 1.3\%$, the uncertainty in the comparison of the internal and external Faraday cups. Other uncertainties were all small compared with the foregoing and are tabulated in Appendix IV. The combined uncertainty on the absolute cross section is $\pm 2.7\%$ for Ni^{58} and $\pm 3.1\%$ for Fe^{58}.

D. ANALYSIS OF THE DATA

D1. Analysis of the Spectra

The spectra were analyzed to obtain cross sections for elastic scattering and inelastic scattering to the first excited state. At higher excitations the energy resolution was not adequate to resolve the more closely spaced states; however, some qualitative remarks will be made on the strongly produced states in Sec. E3.

Two methods were used to analyze the spectra: a full graphical analysis, and for the majority of spectra a simplified peak-height method. These methods are described in detail in the next two sections.

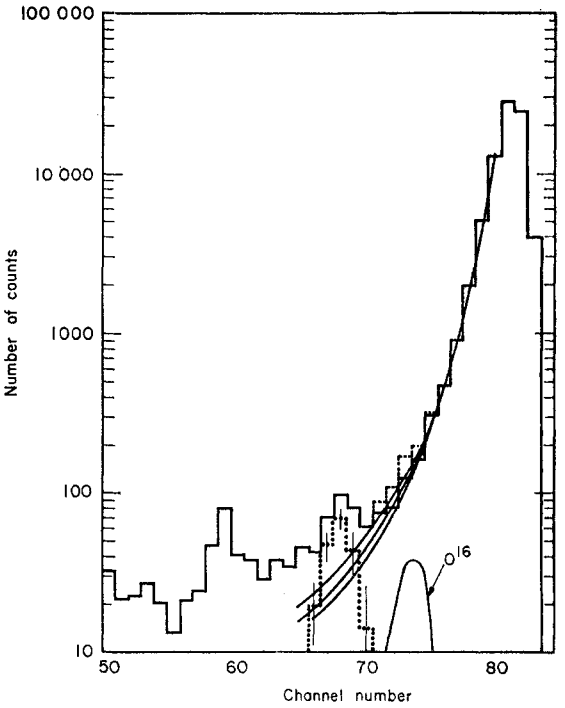

FIG. 6. A Ni^{58} spectrum (solid line histogram) at $\theta_{c.m.}=13.75°$. The contribution of the oxygen contaminant is shown and the spectrum (dashed line histogram) with oxygen subtracted off. The first-excited-state peak is shown (dotted line), and three power-law tails (solid curves).

Each operation in the analysis of the data was performed twice, by different people, as a check against bias and numerical errors. Where discrepancies occurred, they were resolved with the assistance of a third person either by eliminating the cause of the discrepancy or by an increase in the assigned uncertainty where appropriate.

D2. Graphical Analysis of Spectra

Spectra were graphically analyzed when necessary, the purposes being the following:

(a) To determine peak shapes accurately for the peak-height method of analysis (see Sec. D3) and for the absolute cross-section measurements.

(b) To eliminate contributions from oxygen and carbon contaminants at certain angles.

(c) To analyze the large-angle spectra where the energy resolution had become very bad and where heavy-element contamination had arisen.

(d) To resolve uncertainties in the peak-height analysis in extreme cases, such as when the first excited state was very small.

In the analysis we were greatly helped by the following considerations:

(a) In the Ni^{58} spectra the ground-state tail had dropped to a low level (0.1% to 0.4% of the ground-state peak height, depending on energy resolution)

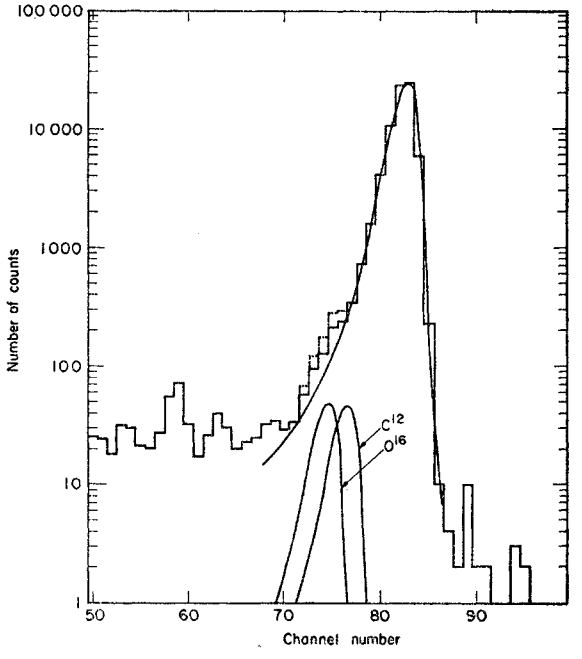

FIG. 7. An Fe^{58} spectrum (solid line histogram) at $\theta_{c.m.}=13.71°$. The contribution of the carbon and oxygen contaminants are shown, and the spectrum (dashed line histogram) with contaminants subtracted. A power-law tail (solid curve) is shown.

at the position of the first excited state and the shape of the tail was, apart from small contributions from oxygen and carbon contaminants, easily determined in between the ground-state and first excited-state positions.

(b) The peak shapes for Ni^{58} and Fe^{58} were so nearly the same that we could use the Ni^{58} shapes to analyze the Fe^{58} spectra.

(c) For making the corrections for carbon and oxygen contaminants we could use the cross sections measured for these elements at 65 MeV by Harvey *et al.*[19]

The following assumptions, verified as far as possible by careful analysis of the spectra, are made in the analysis:

(a) The peak shapes are, apart from distortions produced by the finite channel width and nonlinearity of the pulse-height analyzer, identically the same for the ground state and first excited state. Even at the largest angles measured, the calculated energy spreads due to kinematics and ionization losses in the target differ by only a few keV for the ground state and first excited state, compared with the energy resolution of a few hundred keV. We have no evidence that the energy resolution of the counters should differ for two particle groups so close in energy.

(b) It was assumed that the shape of the ground-state tail as determined fron a Ni^{58} spectrum was a good guide to the shape of the ground-state tail for Fe^{58} in the region of the first excited state at 0.8 MeV. This assumption is justified by our experimental procedure. Firstly, the beam intensity and target angle were kept fixed for consecutive Ni^{58} and Fe^{58} spectra. Secondly, the stopping powers of the two targets were almost exactly the same. Thirdly, the cross sections for the two elements are so similar at all angles that the counting rates for fixed beam intensity were nearly the same.

The only reasons discovered to invalidate this assumption when applied to consecutive runs at the same angle became obvious in the analysis: A slight gain shift during one of the runs could distort the peak; and for the largest angles, where the energy loss in the target became an important contributor to the resolution, it became necessary to give spectra from the two elements completely separate treatment.

(c) The contaminant peaks were assumed to have the same shape as the Ni^{58} and Fe^{58} peaks. This is not precisely true since for the light elements the kinematic energy spread across the finite acceptance contributes to the energy spread. The corrections applied because of these peaks were, however, extremely small in most cases and the failure of this assumption has negligible effect on the results.

Figure 6 shows a Ni^{58} spectrum in which the ground state to first excited state ratio is about 500. The contribution of the oxygen contaminant is shown and subtracted from the spectrum. The smooth curves drawn through the ground-state tail have the form

$$N=N_0c^{-n},$$

where N is the number of counts in a channel c channels

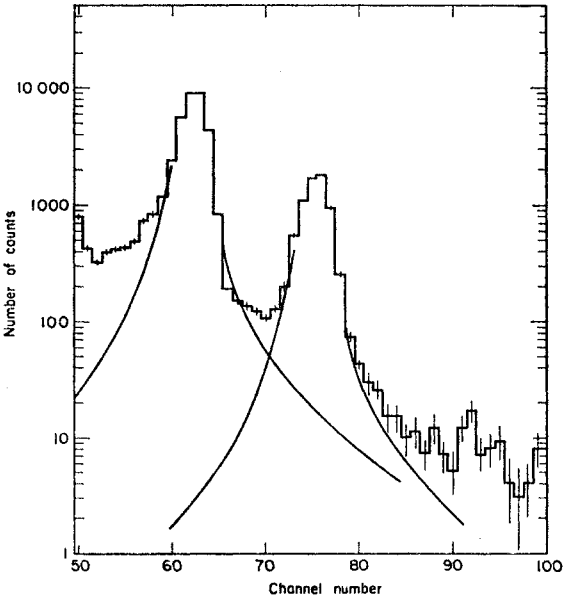

FIG. 8. A Ni^{58} spectrum at $\theta_{c.m.}=25.91°$. Tail shapes obtained by an iterative procedure are shown.

[19] B. G. Harvey, E. J.-M. Rivet, A. Springer, J. M. Meriwether, W. B. Jones, J. H. Elliott, and P. Darriulat, Nucl. Phys. (to be published).

from the ground-state peak and N_0 is a parameter determined by fitting the channels in the region 400–500 keV below the peak. This form of tail could always be fitted within the statistical uncertainty while n is varied from 3.0 to 3.6 depending on the energy resolution. Note that this shape of tail falls much less rapidly than a Gaussian shape while the high-energy side of the peak is in this spectrum consistent with a Gaussian shape.

This parametrization of the tail shape was used to calculate the number of counts in the part of the tail obscured by the remainder of the spectrum. The addition made a contribution varying from 0.25% to 0.45% of the ground-state intensity for Ni^{58} and from 0.4% to 0.8% for Fe^{58}.

Figure 7 shows the Fe^{58} spectrum at the same angle, the ratio of ground state to first excited state being here about 250. In the Fe^{58} target we had both oxygen and carbon contaminants; their contributions are shown. After subtracting the contaminant peaks the ground-state tail has been fitted by superimposing the Ni^{58} spectrum. In order to do this it was necessary to make a small correction to allow for the finite channel width of the analyzer. Since in this spectrum the full width at half-maximum of the peak is about 2.5 channels, the number of counts in the maximum channel depended on the exact part of the channel in which the peak occurred. This correction was normally less than 10%.

After subtracting the ground-state tail, the remaining counts were plotted to see that they were consistent with the correct shape for the first excited state. For this spectrum the uncertainty in the cross section for the first excited state is quoted as $\pm 25\%$ of which $\pm 10\%$ is the contribution of the statistics.

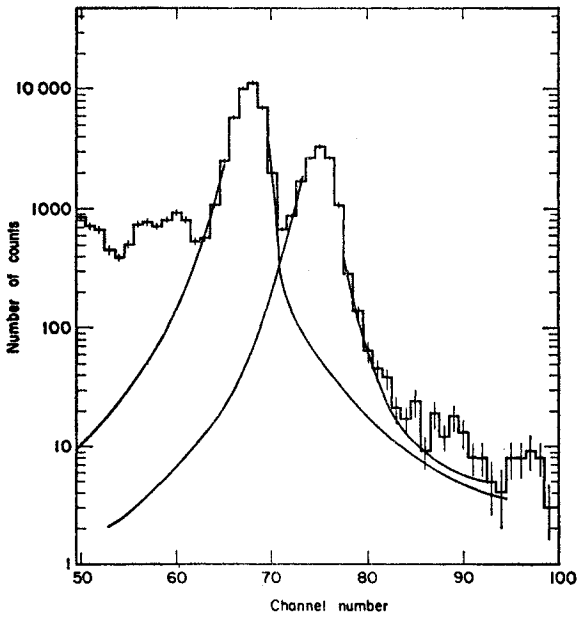

FIG. 9. An Fe^{58} spectrum at $\theta_{c.m.} = 25.91°$. Tail shapes obtained by an iterative procedure are shown.

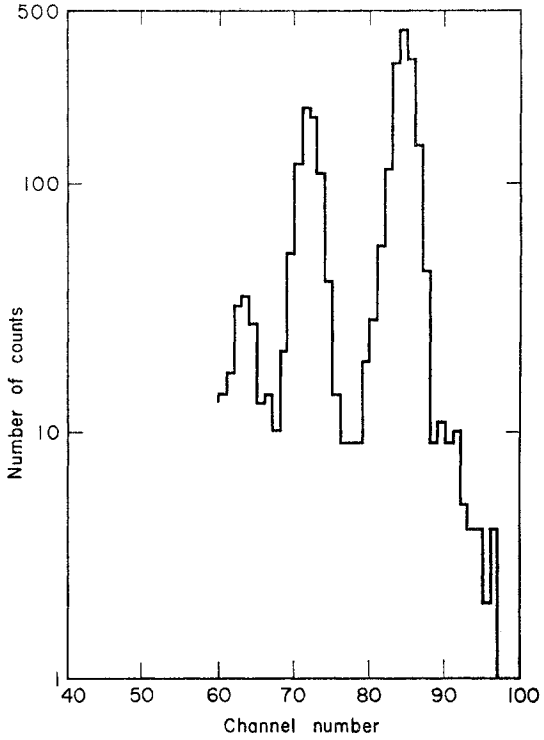

FIG. 10. A Ni^{58} spectrum at a large angle, $\theta_{c.m.} = 64.23°$.

Figures 8 and 9 show the graphical analysis of another pair of spectra with worse energy resolution and a very different ratio of the two states. In these examples the tail shapes were obtained by an iterative procedure requiring that the shapes should be the same for the ground state and first excited state. Note that in these spectra the low-energy tail is still consistent with a power-law curve but that the power is lower than in the previous examples. In addition, we have a high-energy tail due to pileup in the electronics.

The uncertainties in the graphical analysis were estimated independently by the persons performing the analysis. In nearly all instances the analyses were consistent within the assigned uncertainty and the two results were averaged for the final cross section.

Figures 10 and 11 show two spectra obtained at a large angle. Here there were no problems due to light contaminants because the energy of scattered particles from oxygen and carbon had dropped out of the region of interest. However, some heavy element contamination had arisen for the iron target (see Sec. C2), the peaks had become much broader and in particular the Fe^{58} peaks had become broader than the Ni^{58} ones so that the Ni^{58} and Fe^{58} spectra had to be analyzed completely independently.

The heavy element contamination is manifested mainly through the presence of cadmium peaks in the

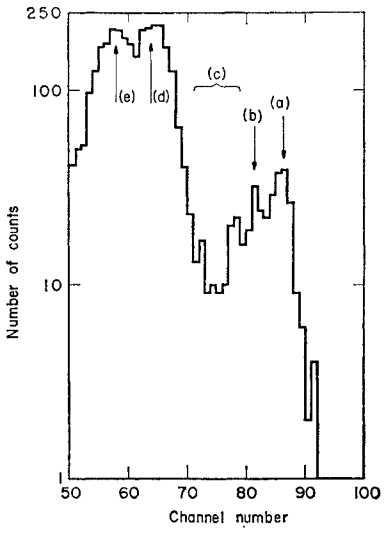

FIG. 11. An Fe^{58} spectrum at a large angle, $\theta_{c.m.}=62.86°$: the ground state of Cd (a), the first excited states of the Cd isotopes ($Q=-0.55$ to -0.65 MeV) (b), and the Cd second excited-state peaks are shown. Also noted are the ground state (d) and first excited state (e) of Fe^{58}.

Fe^{58} spectra. No evidence of it is found in the Ni^{58} spectra nor in the Fe^{58} monitor spectra at 43.5°. The contribution of the contaminant in the region of the peaks being analyzed is small compared with the statistical uncertainty and still smaller compared with the uncertainty in the analysis of the Fe^{58} spectra as can be seen from example in Fig. 11. To allow for it, a correction of about 1% was subtracted from the cross sections and the uncertainty was increased by 1%.

The large angle Ni^{58} spectra show no serious problems for graphical analysis (see Fig. 10); the results of graphical analysis and analysis by the peak-height method agree within the statistical uncertainties. The Fe^{58} spectra are more difficult because of the considerable overlap of the ground-state and first excited-state peaks and therefore the peak-height method was inapplicable. The two states were fitted with peaks of the same shape and an analysis uncertainty was estimated using the peak-to-valley ratio as a criterion. This uncertainty varies from 10–20% compared with statistical uncertainties of 3–6%.

D3. Peak-Height Analysis of Spectra

The peak-height method was developed for several reasons:

(a) It was impracticable to analyze over four hundred spectra graphically.

(b) A systematic procedure was required which would give internal consistency to the results.

(c) The only least-squares program available was limited to fitting Gaussian peak shapes whereas our peaks had a marked low-energy tail.

The large majority of our spectra were analyzed by the peak-height method. The only disadvantage of this method lies in a slight worsening of statistical accuracy; since our statistics were usually extremely good, this was a small price to pay for the convenience of the method.

TABLE I. Definitions of quantities in the peak-height analysis method.

Quantity	Definition
η_g	Height of ground-state maximum.
η_f	Height of first excited-state maximum.
$\Delta\eta_g$	Contribution of first excited state at position of ground-state maximum.
$\Delta\eta_f$	Contribution of ground state at position of first excited-state maximum.
m	Number of counts in a channel four channels below the first excited-state maximum.
m_g and m_f	Contributions to m of the ground-state and first excited-state tails, respectively.
S_0	Number of counts recorded at energies higher than that corresponding to m, excluding m.
ΔS_g and ΔS_f	Number of counts excluded from the ground-state and first excited-state peaks by this process.

A number of spectra were analyzed graphically and classified according to energy resolution. Various quantities related to the peak shape were plotted as a function of the energy resolution.

Figure 12 is a schematic spectrum with the corrections greatly exaggerated, to show the nomenclature used. In Table I the symbols in Fig. 12 are defined. It is assumed that the ground-state and first excited-state peaks have exactly the same shape apart from distortions produced by the analyzer channel width and nonlinearity; even at the largest angles measured, the energy spreads introduced by ionization losses in the target differ by only a few keV for the two states, and we have no evidence that the resolution of the counters should differ for two particle groups so close in energy. It can be seen that when the corrections $\Delta\eta_g$ and $\Delta\eta_f$ are suf-

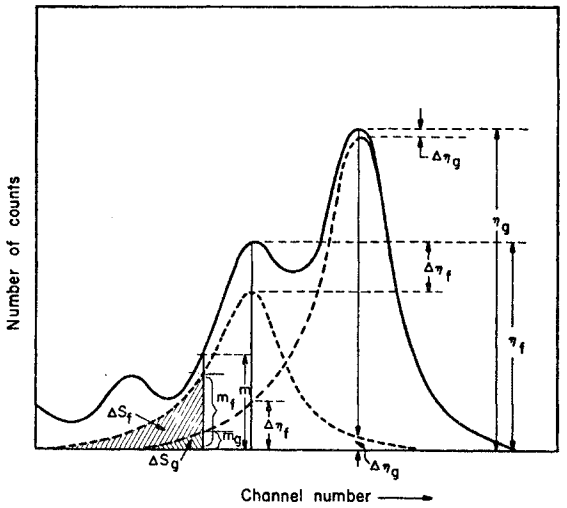

FIG. 12. Schematic spectrum illustrating the peak-height method for separation of the ground state and the first excited state from a pulse-height spectrum. The spectrum is considerably distorted to display the corrections.

ficiently small that the slopes of the tails do not appreciably distort the peak shapes, the number of counts N_g and N_f in the ground-state and first excited-state peaks are as follows:

$$N_g=(S_0+\Delta S_g+\Delta S_f)\frac{\eta_g-\Delta\eta_g}{\eta_g-\Delta\eta_g+\eta_f-\Delta\eta_f}, \quad \text{(D3.1a)}$$

$$N_f=(S_0+\Delta S_g+\Delta S_f)\frac{\eta_f-\Delta\eta_f}{\eta_g-\Delta\eta_g+\eta_f-\Delta\eta_f}. \quad \text{(D3.1b)}$$

Since the peaks had full widths at half-height of only three to four channels, it was necessary to use a special procedure to find η_g and η_f. For each maximum a parabola was fitted to the three central channels in such a way that the number of counts in each channel was correctly given by the area under the parabola.

If A, B, and C are the number of counts in the three central channels we find

$$\eta=B+\rho[(C-A)/2]+\tfrac{1}{12}[B-\tfrac{1}{2}(A+C)], \quad \text{(D3.2)}$$

where the maximum of the parabola is shifted from the center of the channel with B counts by an amount ρ where

$$\rho=\tfrac{1}{4}[C-A]/[B-\tfrac{1}{2}(A+C)]. \quad \text{(D3.3)}$$

An energy-resolution function R was defined as follows:

$$R=\frac{\eta_g-\Delta\eta_g+\eta_f-\Delta\eta_f}{S_0+\Delta S_g+\Delta S_f}\approx\frac{\eta_g+\eta_f}{S_0}. \quad \text{(D3.4)}$$

The approximation was sufficiently accurate in all cases.

Plots were made of $\Delta S_g/\eta_g$ versus m_g/η_g and $\Delta S_f/\eta_f$ versus m_f/η_f for various values of R. This choice of parameters for plotting eliminated the uncertainty introduced in the definition of m. Depending on the exact position of the first excited-state peak relative to the nearest analyzer channel, m might vary from 3.5 to 4.5 channels away from the peak. Plots were also made of $\Delta\eta_g/\eta_f$ and $\Delta\eta_f/\eta_g$ as a function of R.

For each spectrum the relationship $m=m_f+m_g$ was checked using calculated values of m_f and m_g from a subsidiary graph. A few spectra where this did not hold were given special treatment. This could be for several reasons:

(a) At certain angles contaminant peaks due to oxygen and carbon obscured the analysis. At such angles the spectra were analyzed graphically.

(b) In some Ni^{58} specrra a peak appeared at about 1.95-MeV excitation (four channels from the first excited state). It is not certain whether this state is a true excited state in Ni^{58} or whether it is due to inelastic scattering in the silicon detector. Where it could be distinguished this peak had an intensity of roughly 0.2% of the elastic peak.

Errors on the corrections ΔS_g, ΔS_f, ΔN_g, and ΔN_f were estimated by comparison with graphical analysis of spectra where these quantities could easily be determined. The true values fluctuated about the calculated values in a fairly random fashion; to include these fluctuations an uncertainty of $\pm 50\%$ was assigned to each correction. This was rarely the dominant contribution to the final error.

The basic statistical uncertainty is somewhat modified by the peak-height method of analysis. It is seen from the equation that η varies between $\eta=(25/24)B-(1/12)A$ when $\rho=0$ and $\eta=(13/12)B+(5/24)C-(7/24)A$ when $\rho=0.5$. Thus the square of the statistical uncertainty $(\Delta\eta)^2$ is equal to η within 10%.

Assuming that the uncertainty in η is $\sqrt{\eta}$, and using the relationship

$$R\approx\frac{\eta_g+\eta_f}{S_0}\approx\frac{\eta_g}{N_g}\approx\frac{\eta_f}{N_f}, \quad \text{(D3.5)}$$

we find $(\Delta N_g)^2=N_gM_g$ and $(\Delta N_f)^2=N_fM_f$, where

$$M_g=\frac{1}{R}+\left(\frac{1}{R}-1\right)\frac{\eta_g}{\eta_g+\eta_f} \quad \text{(D3.6a)}$$

and

$$M_f=\frac{1}{R}-\left(\frac{1}{R}-1\right)\frac{\eta_f}{\eta_g+\eta_f}. \quad \text{(D3.6b)}$$

Thus, when $\eta_f\to 0$, $M_g\to 1$, and $M_f\to 1/R$ so that $(\Delta N_g)^2\to N_g$ and $(\Delta N_f)^2\to N_f(N_f/\eta_f)$, while when $\eta_g\to 0$, $(\Delta N_g)^2\to N_g(N_g/\eta_g)$, and $(\Delta N_f)^2\to N_f$.

Since the ground state was for most of our measurements much more intense than the first excited state, the ground-state uncertainties have been very little changed. Of the spectra analyzed by the peak-height method, in over half the cases the ground-state error was increased by less than a factor of 1.05 and in three quarters by less than 1.25, while the first excited-state statistics were in most cases worsened by a factor of from 1.5 to 2.0.

An over-all correction has to be made to the results of the peak-height method of analysis to allow for nonlinearity of the pulse-height analyzer. Since the height of a peak is directly proportional to the energy width of the analyzer channel at which it falls, this was an important correction since the analyzer was seriously nonlinear. Evidence from the spectra gave the relative channel widths for the ground state and first excited states to an accuracy of $\pm 2\%$. This correction (up to 6% for Ni^{58} and 3% for Fe^{58} depending on the position of the spectrum on the analyzer) is a correction to the *ratio* N_g/N_f. Where the ratio is large (or small) its effect and its uncertainty are felt mainly on the smaller of N_g and N_f (in most cases only on the first excited state).

D4. Analysis of the Monitor Data

(*a*) *General considerations.* The assumption for use of the monitor data is that the principal fluctuations of

beam position and angle occur in the horizontal plane. This is expected since all the beam-direction controls operate in the horizontal plane. No evidence for vertical fluctuations of the beam was found during the experiment.

If the two monitor counters are set at exactly the same angle on either side of the mean beam direction in an angular region where the cross section is varying as a function of angle, the ratio between their counting rates gives a measure of the deviation of the beam from its mean position while the sum of the two counting rates is to first order independent of beam fluctuations in the horizontal plane. If the counters are not at *exactly* the same angle, it is possible, provided that the rate of change of the cross section with angle has the same sign both, to choose a linear combination of the two counting rates that is independent of the beam position.

The number of monitor counts was determined in a uniform fashion by cutting off the pulse-height analysis spectrum a fixed number of channels below and above the ground-state peak, in such a way as to include the contributions of the ground state and first excited state. The fluctuations that could be introduced by small gain shifts (half the number of counts in the cutoff channel) were $\pm 0.1\%$, $\pm 0.15\%$, and $\pm 0.2\%$ for the 15°, 27°, and 43.5° monitor settings, respectively. The cross sections for the selected events will be referred to as σ_L and σ_R and the linear combination independent of angle as $(\sigma_L + \lambda\sigma_R)$.

To determine the parameter λ it is necessary to know the relative counting rates and the slope of the differential cross section for the two monitors when the beam is in its mean position. Since the monitor angles had no fine adjustment, this could not be done directly, but it could be obtained by using data from the movable counters. Since the angular resolution was very nearly the same for the monitor and movable counters, there can be no distortions involved in the comparison. To determine the monitor angles we calculated from each monitor spectrum the ratio σ_{gs}/σ_{fe} of the ground-state cross section σ_{gs} and the first excited state cross section σ_{fe}. This ratio changes about twice as rapidly as either σ_{gs} or σ_{fe} at most angles and its use eliminates normalization difficulties.

(*b*) *15° monitors.* At the 15° monitor settings σ_{gs} and σ_{fe} changed by about 1% for an angle change of 0.01° while the ratio σ_{gs}/σ_{fe} changed by about 2%. From an analysis of σ_{gs}/σ_{fe} for all the runs it was found that the angles as seen by the monitors had a rms fluctuation of $\pm 0.04°$ about the mean position. For consecutive runs the rms fluctuation was $\pm 0.015°$. The linear combinations used for the monitors were $(\sigma_L + 2.17\sigma_R)$ for Ni^{58} and $(\sigma_L \pm 2.15\sigma_R)$ for Fe^{58}. The large values for λ are principally due to the fact that the accuracy in placing the monitor counters was not very good and their angles differed by about 0.7° so that the counting rates were very different.

The values of λ were uncertain to $\pm 14\%$ due to uncertainty in the angular dependence of the cross sections; this would cause fluctuations in $\sigma_L + \lambda\sigma_R$ of $\pm 0.25\%$ for beam fluctuations of $\pm 0.04°$. Note that with $\lambda = 0$ or $\lambda = \infty$ the fluctuations would be $\pm 4\%$, and with $\lambda = 1$ we would have $\pm 1.5\%$.

(*c*) *27° monitors.* Here the monitor angles were much closer to a maximum of the ground-state cross section so that less angular information could be obtained. From the ratio σ_{gs}/σ_{fe} the angles for each run could be determined to an accuracy of $\pm 0.05°$. After unfolding this uncertainty from the data the over-all rms fluctuation of monitor angle was again found to be $\pm 0.04°$.

This angular fluctuation of the monitors would be completely explained if the centroid of the beam intensity at the target position fluctuated horizontally by ± 0.006 in.; it could equally be explained by an angular fluctuation without lateral movement of the target spot. The fluctuation may be compared with the size of the beam-defining collimator which was a 0.094-in.-diam circle.

The multipliers λ were chosen as unity for both targets for this monitor setting. For $\pm 0.04°$ beam fluctuations the monitor uncertainty would be less than $\pm 0.1\%$.

(*d*) *43.5° monitors.* Because of obstruction by a supporting pillar in the chamber one of the monitor counters had to be placed much nearer the target for this setting.

The sensitivity of σ_{gs}/σ_{fe} to θ was sufficient to determine the angles to $\pm 0.1°$, not enough to give information on fluctuations of the beam position. Both σ_L and σ_R were almost completely insensitive to angle. The factor λ was taken as 1.63 for Fe^{58} and 1.59 for Ni^{58}; most of the difference from unity is due to the difference in solid angles of the two counters. For the counters individually, fluctuations of $\pm 0.04°$ would produce less than 0.1% change in counting rate. For $(\sigma_L/\lambda\sigma_R)$ the effect should be even less.

Late in the run one of the monitor counters began to pass increased current and eventually failed. Before it broke down completely, its resolution became progressively worse. Despite the above results on lack of sensitivity to angle, it was felt unwise to rely on one monitor only. The two monitor counting rates were therefore compared with the beam currents as measured by the Faraday cup for the runs when both monitors were functioning and the single monitor for the remaining runs. The ratio σ_L/σ_R was constant within the rather poor statistical accuracy while for a single monitor the ratio of monitor counts to integrated beam fluctuated by $\pm 1.7\%$ for Fe^{58} and $\pm 2.0\%$ for Ni^{58}. While this fluctuation is probably mainly due to differences in target thickness for repeated settings of the target height, it was decided to rely on the single monitor but to combine the above uncertainties with the statistical uncertainty as a safety factor. The effect of this procedure was to increase the over-all uncertainty by a factor about 1.1 for Ni^{58} and by a negligible amount for Fe^{58}.

(*e*) *Relative normalization of the monitors.* To normalize the 27° and 43.5° settings, measurements were made at six angles in the neighborhood of the ground-state maximum at 35° before and after the monitor positions were changed. Each pair of runs gave a value for the normalization factor with a statistical accuracy between 1% and 2%. To allow for the fact that the counter angles had been reset with an uncertainty of ±0.05° the statistical uncertainty on each point was increased by an amount depending on the slope of the differential cross section as determined from a smooth curve drawn through the points. Using this combined uncertainty a χ^2 test was applied to test the six values for consistency. The weighted mean normalization factor had an uncertainty of ±0.76% for Fe^{58} and ±0.74% for Ni^{58}.

To normalize the 15° setting to the 43.5° setting a different procedure was used. One of the movable counters was fixed at 19.5°, near a maximum of the ground-state cross section. Then measurements were made with the other counter at three angles near the 19.5° maximum (a region which had been studied with the 15° monitor setting). The monitor counters, in the 43.5° setting for these measurements, accumulated rather poor statistics because for the high counting rates near 19° the beam intensity had to be reduced.

Use was made of the conclusion in Sec. D4d, that the monitor counters at 43.5° are very insensitive to fluctuations of the beam angle, to permit combination of all the measurements of the fixed counter relative to the 43.5° monitors. This gave a normalization factor enabling us to use the fixed counter at 19.5° in lieu of the 43.5° monitor. Various χ^2 tests were made confirming the consistency of this procedure.

Since the three angles measured were not, because of the beam shift which had occurred during the run, exactly the same as those measured with the 15° monitor, the normalizations had to be obtained graphically. Two degrees of freedom were allowed: the normalization factor and the angular shift. The latter had in addition to be the same for Fe^{58} and Ni^{58}. The normalization is rather insensitive to the size of the beam shift and had an uncertainty of ±0.9% for Ni^{58} and ±0.7% for Fe^{58}, determined by considering extreme cases. Figures 13 and 14 show the points used to obtain the two normalizations.

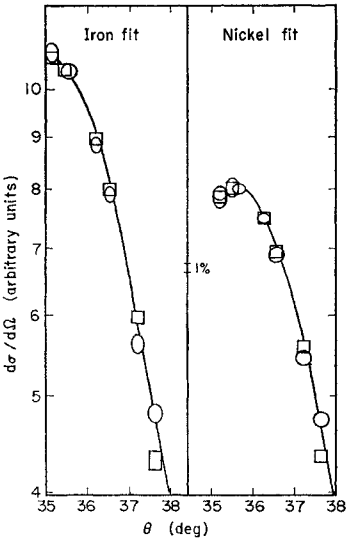

FIG. 13. Data near the ground-state maxima at a laboratory scattering angle $\theta \cong 35°$, taken before (□) and after (○) moving the monitor counters from ±27° to ±43.5° which was used to normalize the 27° monitor data to the 43.5° monitor data. The lines drawn through the points illustrate the effect of the angular errors but was not present when the fits were made.

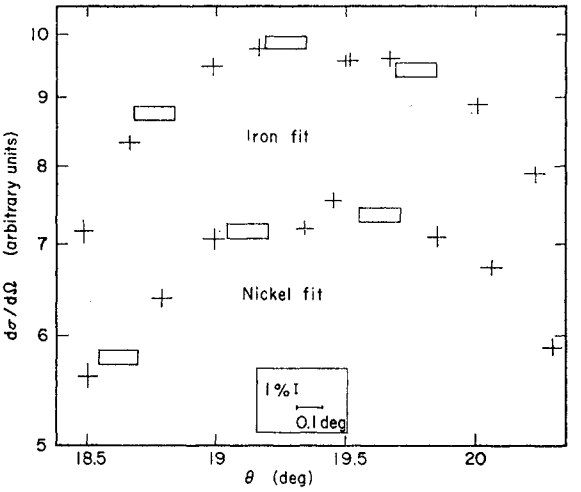

FIG. 14. Data near the ground-state maxima of Ni^{58} and Fe^{58} at a laboratory scattering angle $\theta \cong 19.5°$, used to normalize the data taken with ±15° monitor settings to data taken with ±43.5° monitor settings. The points denoted by the symbol (+) were taken with the monitors at ±15°; those with the symbol (□) at ±43.5°.

(*f*) *Absolute cross-section normalization.* As described in Sec. C3, a special series of angular measurements, the "*C*" runs, were made with Fe^{58} and Ni^{58} foil samples taken from the same material used for the relative cross-section measurements. We discuss here the fitting procedure leading to the normalization of the relative cross-section data to the "*C*" data. Six "*C*" measurements for each target were made near the 19.5° maximum ($\leq 0.5\%$ statistical uncertainty on each data point). The top counter data for Ni^{58} and Fe^{58} "*C*" runs and the corresponding bottom counter data were plotted separately and fitted to one another to obtain a relative angular shift and a relative normalization, and then combined into one plot with the top and bottom data points properly normalized and shifted with respect to one another. The angular shift and normalization which were found by this procedure were compatible with the values of these obtained in the relative cross-section data when the error resulting from the beam misalignment uncertainties (see Appendix II) and from the solid angle uncertainty (see Appendix IV) were taken into account. The resulting "*C*" data were then fit to the relative cross-section data in the vicinity of the 19.5° maximum as shown in Fig. 15. The uncertainty in fitting the "*C*" data to the relative cross-section data

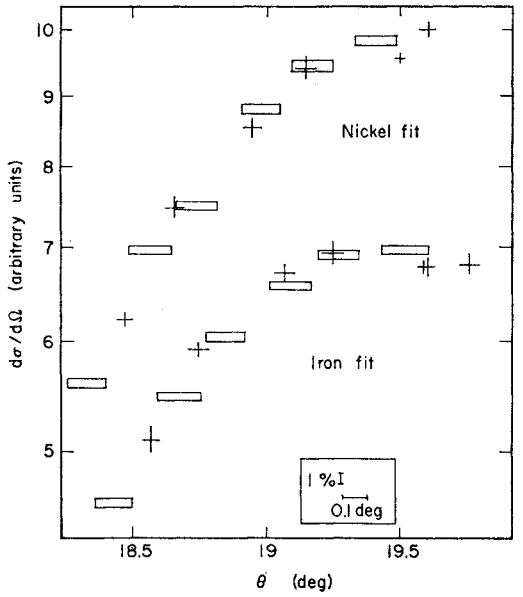

FIG. 15. The relative cross-section data (+) used to obtain the absolute cross-section normalization. The data points denoted by (□) are absolute cross-section measurements.

includes both the statistical uncertainty and the error in fitting as determined by finding the extreme relative shifts of the "C" and relative cross-section data possible. These uncertainties were $\pm 0.35\%$ for Ni^{58} and $\pm 0.17\%$ for Fe^{58}.

E. RESULTS

E1. Differential Cross Sections

The differential cross sections for elastic scattering and excitation for the first 2+ state for Ni^{58} and Fe^{58} are shown in Fig. 5. Numerical values may be found in UCRL Report No. 11054 which is available on request.

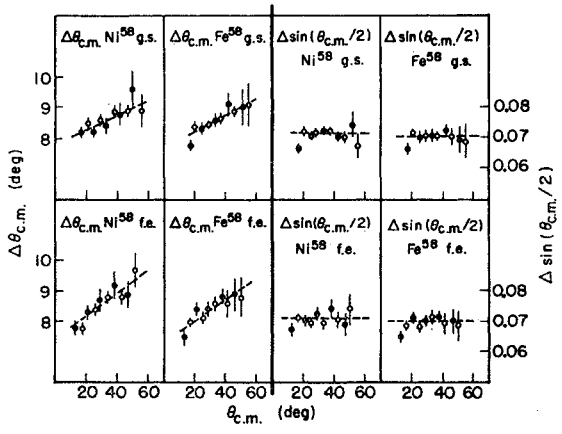

FIG. 16. The angular spacings $\Delta\theta_{c.m.}$ and spacings in $\sin\theta_{c.m.}/2$ between consecutive maxima (○) and consecutive minima (●) in the angular distributions, plotted against the angle of the maximum or minimum nearer zero degrees.

The mean energy of the beam in the targets was 64.3 ± 0.5 MeV and the energy spread due to the target thickness was 0.5 MeV. The corrections which have been applied to the data are summarized in Appendix IV. The angular uncertainties shown in Fig. 5 do not include the contribution due to the beam-misalignment parameter uncertainties since this contribution is systematic for all the angular measurements. It is always less than 0.2 deg and is discussed in Appendix II. The uncertainty in the absolute cross sections is $\pm 2.7\%$ for Ni^{58} and $\pm 3.1\%$ for Fe^{58} (see Sec. C3). The angular resolution function has not been unfolded. It is a function of angle and is usually about 0.5° full width at half-height (see Appendix III). The cross sections have not been corrected for the presence of other isotopes. The Ni^{58} target was 99.25% Ni^{58} and 0.75% Ni^{60} while the Fe^{58} target was 82.04% Fe^{58}, 15.62% Fe^{56}, 1.89% Fe^{57}, and 0.45% Fe^{54}. For comparison with theory, corrections were made to the calculated cross sections for the presence of Fe^{56} (see Sec. F2).

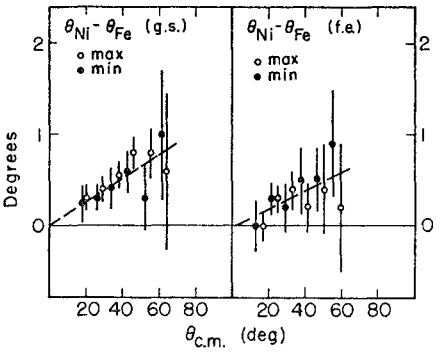

FIG. 17. The differences $\theta_{max}(Ni^{58})-\theta_{max}(Fe^{58})$ (○) and $\theta_{min}(Ni^{58})-\theta_{min}(Fe^{58})$ (●) between corresponding maxima and minima in the differential cross sections, plotted against the angle of the maximum or minimum.

The angular distributions all show marked diffractional behavior, the inelastic cross sections being "out-of-phase" with the elastic scattering, as predicted by Blair[20] for a one-phonon excitation process. The angular spacing between maxima and between minima (see Fig. 16) increases from about 8° at small angles to about 9° at large angles; the spacing in terms of $\sin\theta_{c.m.}/2$ (proportional to the momentum transfer) is much more constant. The positions of the maxima and minima for Ni^{58} occur at slightly larger angles than for Fe^{58}. The differences are displayed in Fig. 17.

Above about 50° the intensities of the elastic and inelastic scattering are comparable while at small angles the elastic-scattering maxima are 5–10 times more intense than those of the inelastic scattering. The ratio of a Ni^{58} elastic maxima to the corresponding Fe^{58} one increases from 1.1 at small angles to 2.0 at

[20] J. S. Blair, Phys. Rev. **108**, 827 (1957).

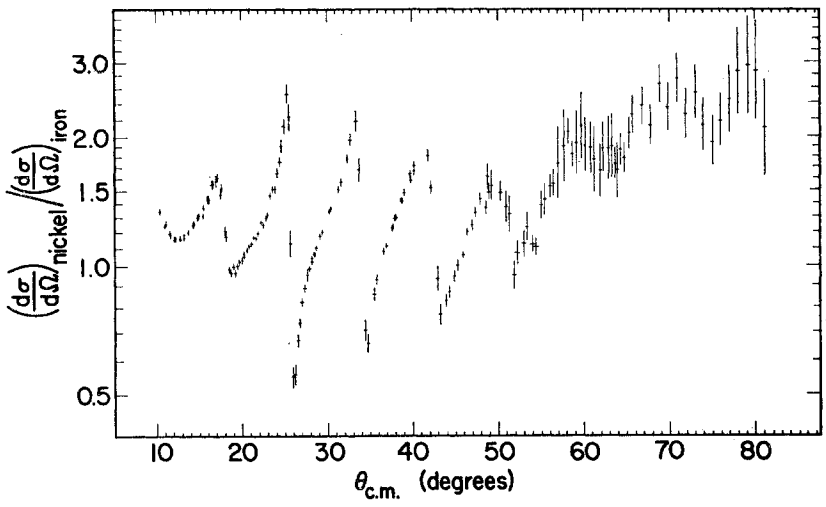

FIG. 18. The ratio $(d\sigma/d\Omega)_{Ni^{58}}/(d\sigma/d\Omega)_{Fe^{58}}$ for the elastic scattering, plotted against the center-of-mass scattering angle.

large angles while the corresponding ratio for the inelastic scattering increases from 0.75 to 1.1 at large angles.

E2. Ratio of Elastic-Scattering Cross Sections

As remarked in the last section, the maxima and minima for Ni^{58} and Fe^{58} do not coincide. The differences between the two isobars are sensitively displayed in the ratio of the elastic-scattering cross sections. This ratio is shown in Fig. 18. Numerical values may be found in UCRL Report No. 11054 which is available on request. The angular error due to beam-misalignment parameter uncertainties is identical to that on the differential cross sections (see Sec. E1). The remarks on the angular resolution function and the isotopic impurity discussed in Sec. E1 apply.

The relationship between the uncertainties in the ratio and in the individual cross sections requires discussion:

(a) The angular uncertainties for Ni^{58} and Fe^{58} are correlated, so the same uncertainty applies to the ratio rather than some larger uncertainty. This is because the angular settings were in general the same for each pair of measurements on Ni^{58} and Fe^{58}; a number of data points where this requirement was not satisfied have been omitted from Fig. 18. The monitor data showed that for consecutive runs the rms shift in angle caused by small fluctuations in the beam position was $\pm 0.015°$. This rms angle shift has been converted into an rms cross-section change by means of the measured angular distributions and the uncertainty on the ratio has been increased correspondingly.

(b) Uncertainties in the solid angles of the two detectors used disappear in the ratio.

(c) Several possible systematic errors in the absolute cross sections disappear, for example, the uncertainty in absolute efficiency of the detectors and of the Faraday cup. The absolute uncertainty in the ratio is $\pm 3.6\%$.

An important feature of the ratio is the rise at large angles, discussed in Sec. F2. It is interesting to note that in the proton-scattering results of Benveniste *et al.*,[9] a similar effect was seen in the comparison of Ni^{58} and Fe^{58}, but not for Ni^{64} and Zn^{64}. Benveniste *et al.* attributed the effect to compound elastic scattering.

E3. Higher Excited States

We have not performed an analysis of the angular distributions for any excited states except the first. To illustrate the energy spectra at higher excitations we

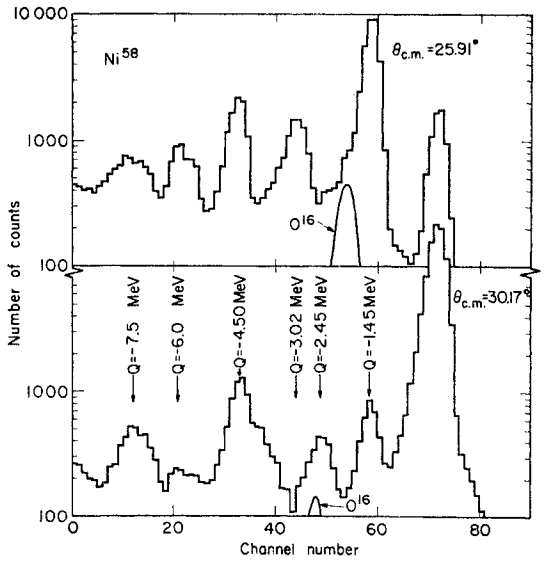

FIG. 19. Ni^{58} energy spectra taken at $\theta_{c.m.}=25.91°$ (near maximum of the first excited-state angular distribution) and $\theta_{c.m.}=30.17°$ (near a maximum of the elastic-scattering angular distribution). To obtain the correct relative normalization of the two spectra the latter should be multiplied by about 1.5.

show in Figs. 19 and 20 spectra taken near adjacent maxima in the angular distributions for the ground state and first excited state, respectively. To obtain the correct relative normalization between the two Ni^{58} spectra or between the two Fe^{58} spectra, the 30.17° spectra should be multiplied by about 1.5 and 2.0, respectively.

The spectra show a number of additional peaks, some of which are clearly complex. Obviously, improved energy resolution is required. It is, however, interesting to note that in the Ni^{58} spectra the $Q=-2.45$-MeV peak is very roughly 2.5 times more intense at $\theta_{c.m.}=30.17°$ (ground-state maximum) than at $\theta_{c.m.}=25.91°$ (first excited-state maximum). This is as expected since a 4+ double-excitation state is known to exist at about this energy, and it should be in phase with the elastic scattering. The $Q=-3.02$-MeV peak, strongly excited at 25.91°, is out of phase with the elastic scattering; a 2+ state is already known at about this energy. The remaining peaks do not show any marked change between the two angles. In the Fe^{58} spectra the peak at $Q=-1.70$ MeV is more intense at 25.91° (first excited-state maximum) than at 30.17° (ground-state maximum). This is in agreement with expectation for the 2+ state existing at about this energy. The other peaks for Fe^{58} have roughly equal intensities at the two angles.

F. THEORETICAL INTERPRETATION OF THE RESULTS

F1. Analysis of the Elastic Scattering Using a Spherical Optical Potential

In this section we use a spherical optical potential to obtain fits to the elastic-scattering cross sections for Ni^{58} and Fe^{58} independently. Then using an average set of nuclear parameters, we attempt to fit the ratio of the Ni^{58} and Fe^{58} angular distributions, first allowing only the charge to be different for the two isobars and then allowing differences in the nuclear parameters one by one.

It should be stressed that the analysis is intended to illustrate only the gross features of the results; we would expect to have to use a considerably more refined model to describe the angular distributions in detail.

The calculations were performed using a computer program[21] with a potential of the form

$$V(r)=V_C(r)+\frac{V}{1+\exp[(r-R)/a]}+i\frac{W}{1+\exp[(r-R)/b]}, \quad \text{(F1.1)}$$

where $V_C(r)$ is the Coulomb potential for a uniformly charged sphere of radius R_C; R is the radial distance r to the half-value of the potential and is the same for the real and imaginary parts of the potential; a and b are diffuseness parameters, not necessarily equal; V and W are the depths of the potentials at the nuclear center.

[21] N. K. Glendenning (private communication).

TABLE II. Parameters of the spherical optical potential for the "best fits" to the Ni^{58} and Fe^{58} elastic-scattering cross sections. The parameters found for Ni^{58} at 43 MeV by Bassel *et al.* (Ref. 11) are given for comparison.

Isobar	$-V$ (MeV)	$-W$ (MeV)	a (F)	b (F)	R (F)
Ni^{58}	44.99	20.91	0.565	0.580	6.08
Fe^{58}	41.22	25.53	0.628	0.585	6.08
Ni^{58} (43 MeV)	47.6	13.8	0.549	0.549	6.14

The elastic-scattering amplitude $f(\theta)$ takes the form

$$f(\theta)=f_C(\theta)+(i/2k)\sum_l e^{2i\sigma_l}(2l+1)\times(1-\eta_l)P_l(\cos\theta), \quad \text{(F1.2)}$$

where $f_C(\theta)$ is the Coulomb amplitude, and σ_l is the Coulomb shift for the lth partial wave, the quantity η_l is the amplitude of the outgoing part of the lth partial wave, and $P_l(\cos\theta)$ is the Legendre polynomial of order l, and k is the relative wave number.

The Ni^{58} data were fitted using a search routine starting from the Ni^{58} parameters found by Bassel *et al.*[11] at 43 MeV.

To fit the Fe^{58} data allowance has to be made for the Fe^{56} present in the target. Since no experimental data were available for Fe^{56} the data were fitted without making any corrections and then, using the parameters

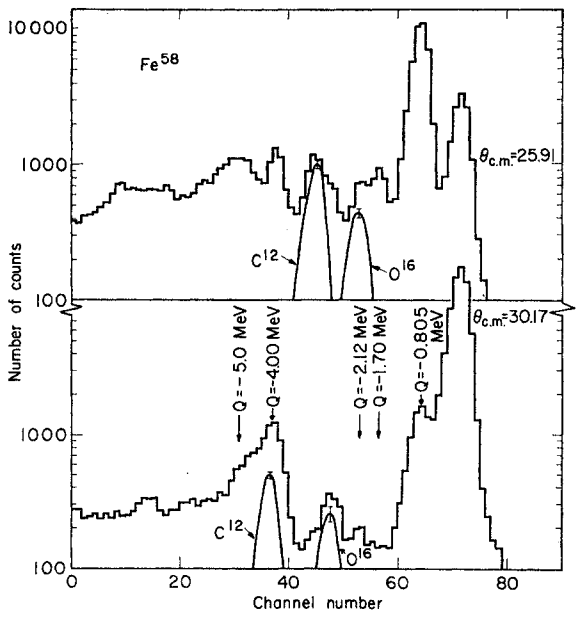

FIG. 20. Fe^{58} energy spectra taken at $\theta_{c.m.}=25.91°$ (near a maximum of the first excited-state angular distribution) and at $\theta_{c.m.}=30.17°$ (near a maximum of the elastic-scattering angular distribution). To obtain the correct relative normalization of the two spectra the latter should be multiplied by about 2.0.

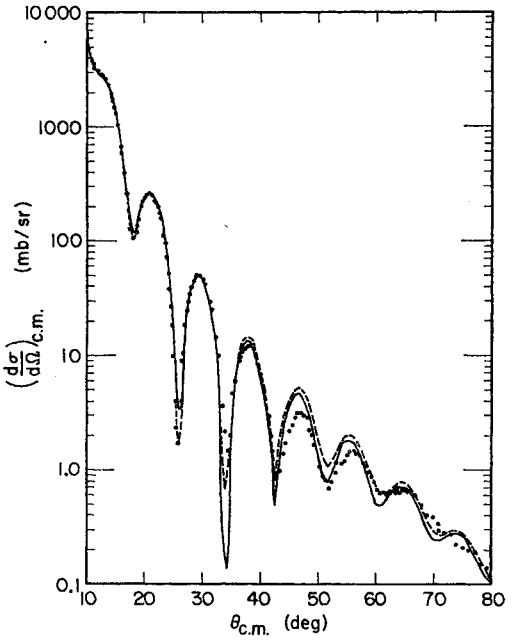

FIG. 21. The "best fit" (——) obtained to the Ni^{58} elastic-scattering cross sections (•) with the optical potential parameters listed in Table II and the fit (dashed line) obtained with $V=-43$ MeV, $a=b=0.58$ F, $R=6.1$ F, and $W=-19.5$ MeV. The uncertainty in the data is apart from a few instances covered by size of spot.

for this fit but multiplying the nuclear radius by $(56/58)^{1/3}$, the angular distribution for Fe^{56} was calculated. The experimental data, corrected using this calculated Fe^{56} cross section, differed by a few percent from the original data mainly near the minima; the corrected cross sections were used for the remaining analysis and in particular the optical-model fit was recalculated.

The "best-fit" parameters for Ni^{58} and Fe^{58} are listed and compared with the 43-MeV Ni^{58} parameters of Bassel *et al.*[11] in Table II. The quantity minimized was not the usual χ^2 but an empirical quantity X^2 developed by Wilkins and Pehl.[22]

The calculated cross sections are compared with experiment in Figs. 21 and 22. It will be noted that the fits are quite good at small angles but become worse at large angles.

To study the effect of the different charges of the two isobars we took various sets of nuclear parameters the same for both nuclei and studied the effect on the ratio of the cross sections of the change in charge. The calculated ratio was almost independent of the nuclear parameters used provided they were the same for both and all within the range between the "best fits" for Ni^{58} and Fe^{58} given in Table II. In Fig. 23 the solid line shows the ratio calculated with the Ni^{58} "best-fit" parameters. It is extremely poor at large angles. To test whether the radial form of the Coulomb potential might differ for the two isobars (Ni^{58} has a closed shell of protons) calculations were performed with R fixed at 6.077 F, and R_c varied between 4.9 and 6.7 F. The differences produced by this variation were negligible even though R_c was varied through a range bigger than that expected from other works.[23] Since the charge difference was insufficient to reproduce the observed ratio of the angular distributions an attempt was made to fit it by changing the nuclear parameters. To find the sensitivity of the various parameters we calculated X^2 for fits in which each parameter was changed by a small amount. If the parameter λ_i differed by $\Delta\lambda_i$ between the Ni^{58} and Fe^{58} best fits (Table II), $(\partial X^2/\partial\lambda_i)\Delta\lambda_i$ gave a measure of the sensitivity of that parameter.

It was found in this way that W was by far the most sensitive parameter; V and a were found to be correlated so that a $+1\%$ change in V had the same effect as a -0.9% change in a.

Therefore, we tried to explain the ratio by varying only W. To do this, we chose an "average" set of parameters: $V=-43$ MeV; $a=b=0.58$ F; $R=6.1$ F and $R_c=4.872$ F. By using $W=-19.5$ MeV (Ni^{58}) and $W=-26$ MeV (Fe^{58}) the fit to the ratio was much improved at large angles (dashed lines in Fig. 23). The fits to the individual cross sections were not so good with these sets of parameters as for the "best fits";

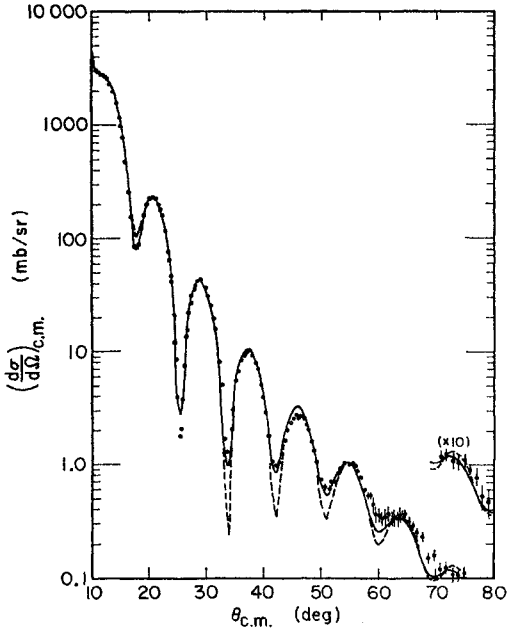

FIG. 22. The "best fit" (——) obtained to the Fe^{58} elastic-scattering cross sections (•) with the optical potential parameters listed in Table II, and the fit (- - -) obtained with $V=-43$ MeV, $a=b=0.58$ F, $R=6.1$ F, and $W=-26$ MeV. The uncertainty in the data is apart from a few instances covered by the size of the spot, except at large angles where the uncertainty is shown.

[22] D. Pehl and B. Wilkins (unpublished).

[23] B. Hahn, D. G. Ravenhall, and R. Hofstadter, Phys. Rev. **101**, 1131 (1956).

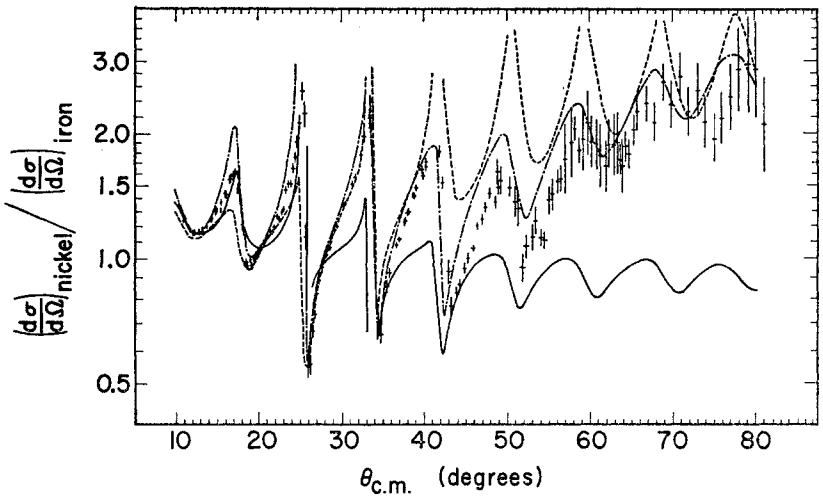

FIG. 23. Optical-model fits to the ratio: $(d\sigma/d\Omega)_{Ni^{58}gs}/(d\sigma/d\Omega)_{Fe^{58}gs}$. (——) $V=44.99$ MeV; $W=-20.91$ MeV; $a=0.565$ F; $b=0.580$ F; and $R=6.1$ F, for both nuclei. This curve is essentially unchanged for any set of parameters within the limits of the "best fits" in Table II. (- - -) $V=-43$ MeV; $a=b=0.58$ F; $R=6.1$ F; and $W=-19.5$ MeV (Ni^{58}) and -26 MeV (Fe^{58}). (—·—) The curve given by the "best fits" of Table II.

they are given by the dashed lines in Figs. 21 and 22. Since the fits to the individual cross sections are not good, no attempt was made to obtain a "best fit" to the ratio by this procedure. In Fig. 23 the ratio given by our "best fits" to the individual cross sections is given for comparison. We may, however, conclude that the differences between the elastic scattering for Ni^{58} and Fe^{58} can be qualitatively explained by (a) a difference in Coulomb scattering and (b) a difference in the absorptive part of the potential.

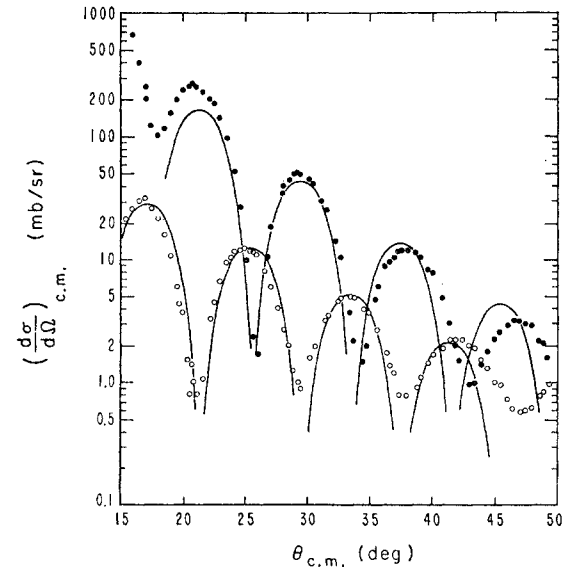

FIG. 24. Fits to the differential cross sections for Ni^{58} obtained using the smooth cutoff model of Blair, Sharp, and Wilets (Ref. 14). The parameters used are $L=22.2$, $\Delta/L=0.054$, and $\beta=0.15$. The experimental uncertainties are omitted for clarity; in the region of the maxima they are smaller than the points: (•) elastic scattering; (○) inelastic scattering to the 2+ first excited state.

F2. Analysis of the Elastic- and Inelastic-Scattering Cross Sections for $\theta_{c.m.}<50°$ Using the Smooth Cutoff Model

The inelastic- and elastic-scattering data in the region of strong diffraction ($\theta_{c.m.}<50°$) has been analyzed using the smooth cutoff calculations of Blair, Sharp, and Wilets.[14] This model neglects the Coulomb potential and assumes that η_l is real and has the form $\{1+\exp[(L-l)/\Delta]\}^{-1}$, where L is the cutoff value of l and Δ is the smoothness parameter. It describes the inelastic scattering in the first order of the nuclear deformation β as an adiabatic process and gives a family of universal curves showing the variation of the dimensionless cross sections $[4k^2/(L+1/2)^4][(d\sigma/d\Omega)(\theta)]_{gs}$ and $[k^2/\beta^2(L+1/2)^4][(d\sigma/d\Omega)(\theta)]_{fe}$ at the maxima of the angular distributions. The angles at which the maxima and minima are predicted to occur are the same as in the sharp cutoff model and are approximately equally spaced in $\theta_{c.m.}$. To fit the data we determined L by fitting the positions of the maxima near $\theta_{c.m.}=30°$ to the values of $(L+1/2)\theta_{c.m.}$ given in Ref. 14 (though examination of our spacing of maxima and minima in Fig. 16 suggests that $2(L+1/2)\sin(\theta_{c.m.}/2)$ might be a more suitable variable). With this value of L we determined Δ/L by fitting the cross sections at the inelastic maxima to the curves in Fig. 10 of Ref. 14. This procedure gave β^2. The angles and absolute cross sections predicted for the elastic and inelastic distributions are compared with experiment in Figs. 24 and 25. The parameters are listed in Table III, where the values of β obtained in other ways are also given for comparison. The agreement is very poor.[24]

[24] *Note added in proof.* Dr. J. S. Blair has pointed out that the more significant quantity is βR_0 rather than β. Numerical values of βR_0 are in much better agreement with corresponding ones obtained from proton data since R_0 for protons is smaller. In addition we have subsequently made more detailed calculation of β. These reveal a 5% uncertainty in β associated with a $\beta^2-\Delta$ ambiguity.

It is interesting to compare the parameters from the smooth cutoff fit with the optical-model results of Sec. F1. In Fig. 26 we show the real and imaginary parts of the quantity η_l as given by the optical-model fit for

TABLE III. The parameters used in the smooth cutoff fit, with other values of β for comparison. (a) (α,α') at 43 MeV (Ref. 14): smooth cutoff analysis. (b) (p,p') at 10.93 MeV (Ref. 10): coupled wave equation analysis. (c) (p,p') at 11.66 MeV (Ref. 10): coupled wave equation analysis. (d) Coulomb excitation (private communication in Ref. 10).

	E (2+)	L	Δ/L	β	β from other experiments (a)	(b)	(c)	(d)
Ni^{58}	1.45 MeV	22.2	0.054	0.15	0.18	···	0.225	0.19
Fe^{58}	0.80 MeV	22.4	0.056	0.17	···	0.246	0.240	0.25

Ni^{58} and the variation of η_l (which is now real) from the smooth cutoff fit.

In Fig. 27 we show the potential for $L=22$ given by the optical-model fit for Ni^{58}. Blair[20] gives a correlation between the smooth cutoff radius R_0 given by

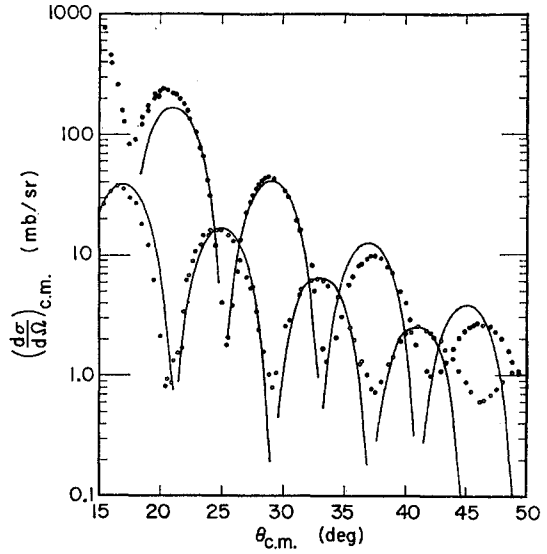

FIG. 25. Fits to the differential cross sections for Fe^{58} obtained using the smooth cutoff model of Blair, Sharp, and Wilets (Ref. 14). The parameters used are $L=22.4$, $\Delta/L=0.056$, and $\beta=0.17$. The experimental uncertainties are omitted for clarity; in the region of the maxima they are smaller than the points: (•) elastic scattering; (○) inelastic scattering to the 2+ first excited state.

$(L+1/2)=kR_0$ and the optical-model potential: The maximum value of the real part of the total potential, nuclear plus centrifugal, for the critical angular momentum L in the surface region is very closely equal to the available energy E. We see from Fig. 27 that this criterion is well satisfied.

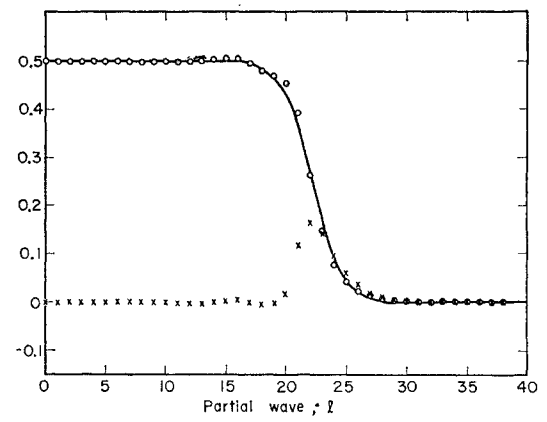

FIG. 26. The real (○) and imaginary (×) parts of $(1-\eta_l)/2$ obtained from the optical-model "best fit" for Ni^{58}, compared with the parameterized form (——) given by $\eta_l=\{1+\exp[(l-L)/\Delta]\}^{-1}$ where $L=22.2$ and $\Delta/L=0.054$.

G. CONCLUSIONS

The main conclusion of this work is the presentation of a high precision measurement of differential cross-section data for elastic and inelastic scattering from $A=58$ isobars. These data are suitable for a careful theoretical study of elastic and inelastic scattering using a coupled equation approach making as few approximations as possible, in which fine detail in the angular distributions must be taken seriously in the fitting process.

Some conclusions have been drawn from the data by

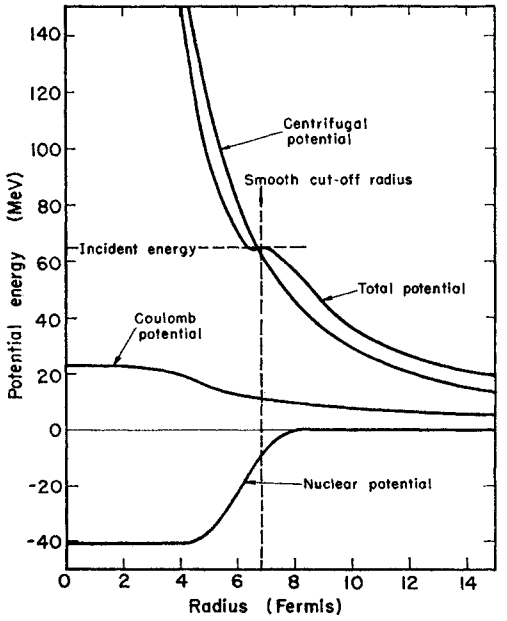

FIG. 27. The Blair criterion for the smooth cutoff radius. The potentials for the 22nd partial wave obtained from the optical-model "best fit" for Fe^{58} add up to the energy of the incident alpha particle at the smooth cutoff radius.

performing simplified analyses. We wish to emphasize that these conclusions do not arise from the precision of the data, but rather depend on the more qualitative aspects of the angular distributions.

The smooth cutoff model of Blair, Sharp, and Wilets[14] gives a fair account of the positions and intensities of the first four maxima of the cross sections. The values of the deformation parameter β found with this model are lower than previously reported. Although it is difficult to estimate the reliability of these values because the theory is quite approximate, the relationship between the values for Ni^{58} and Fe^{58} may be more trustworthy. The deformation parameter β is smaller for Ni^{58} which also has a closed shell of protons.

The optical-model analysis of the elastic scattering gave fair fits to the data. The Coulomb potential difference will not account for the differences between Ni^{58} and Fe^{58} elastic scattering and to explain the behavior of the cross sections at large angles it appears to be necessary to use a deeper absorption potential for Fe^{58} than for Ni^{58}. It has been remarked before[4] that a nonzero value of β requires a greater depth for both real and imaginary parts of the potential if the coupling of the ground state and first excited state is neglected. This serves to emphasize the necessity for a coupled equation approach as used in the later work of Benveniste *et al.*[10]

ACKNOWLEDGMENTS

The authors would like to thank Elmer Kelly for supervising the design and construction of the cyclotron, Hermann Grunder and the cyclotron staff for its efficient operation, Henry Dea for designing the scattering chamber, Jack Elliott for supplying solid-state detectors, and Hugo Atterling for carrying out the beam optics calculations.

We would like to thank Dr. Louis Rosen of the Los Alamos Scientific Laboratory for kindly loaning target materials.

APPENDIX I: DEFINITIONS OF GEOMETRICAL QUANTITIES AND SYMBOLS, AND NUMERICAL VALUES

Definitions of geometrical quantities are given below:

Quantity	Definition
Chamber axis	Common axis of rotation of the top and bottom counters.
Counter planes	Two planes perpendicular to the axis of the chamber containing the centers of the counter collimators.
Equatorial plane	Plane perpendicular to the chamber axis and equidistant from the counter planes.
Meridian plane	A plane containing the chamber axis.
Center line	Intersection of the equatorial plane with the meridian plane containing the scale zeros.
Target plane	The meridian plane perpendicular to the center line.

TABLE IV. Symbols and their definitions used in the text. The subscript 0, when added to a symbol, indicates that the quantity is defined with respect to a beam traveling along the center line.

Symbol	Corresponding quantity
xOy	Equatorial plane.
xOz	Target plane.
C	Center of the counter collimator.
M	Center of the beam spot.
θ	Actual scattering angle.
θ_H	Projection of θ on xOy.
θ_v	Projection of θ on xOz.
$(\xi,0,\zeta)$	Coordinates of M.
$(\alpha,1,\beta)$	Coordinates of a unit vector in the direction of the incident beam.
ψ	Angle between OC and the equatorial plane.
L	Distance between M and C.
h	Distance between the equatorial palne and the counter planes.
a	Width of the counter collimator.
b	Height of the counter collimator.
S	Area of the counter collimator.

I2. Symbols

Figure 28(a) shows a view of the geometry for scattering; Fig. 28(b), a projection on the meridian plane containing the center line; and Fig. 28(c), a projection on the equatorial plane. The symbols listed in Table IV have been used to designate the corresponding quantities. Numerical values are given in Table V.

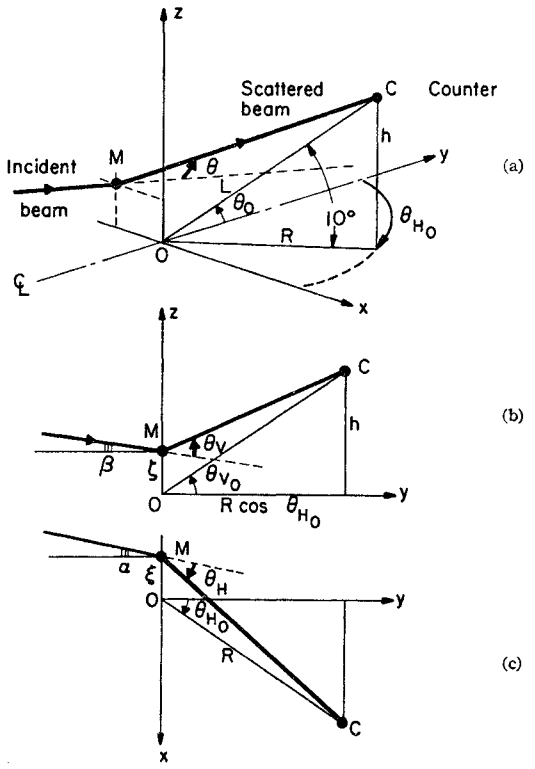

FIG. 28. (a) An isometric view of the scattering geometry. (b) A projection on the meridian plane containing the center line. (c) A projection on the equatorial plane.

TABLE V. Table of numerical values.

Quantity of symbol	Numerical value	Explanatory note
ψ	$10°\pm0.01°$	
L	16.369 ± 0.004 in. T 16.374 ± 0.004 in. B	The top counter (T) and bottom counter (B) values are listed.
a	0.172 in. T 0.172 in. B	a and b dimensions (interchanged for angles greater than 120° in the laboratory system).
b	0.065 in. T 0.068 in. B	
S	$(1.122\pm0.006)\times10^{-2}$ in.^{2} T $(1.168\pm0.006)\times10^{-2}$ in.^{2} B	
$\Delta_{B\xi}$	$2/32\pm1/64$ in.	Horizontal beam spot size.
$\Delta_{B\zeta}$	$3/32\pm1/32$ in.	Vertical beam spot size.
$\Delta_{B\alpha}$	0.0028 ± 0.0014	Radial angular divergence of the beam with X collimator at 0.100 in.
	0.0058 ± 0.0028	Radial angular divergence with X collimator open.
$\Delta_{B\beta}$	0.0014 ± 0.0007	Vertical angular divergence.

APPENDIX II: FIRST-ORDER CORRECTION DUE TO MISALIGNMENT OF THE BEAM

Since α, β, ξ, and ζ are nonzero, two kinds of corrections must be made. First, angular corrections due to differences between θ and θ_0; and, second, solid-angle corrections due to differences between L and L_0. The former mask the latter on the sides of maxima in the angular distributions. The latter show up at the maxima where angular corrections have no effect. In what follows, expressions for these two corrections have been written down to first order in α, β, ξ/L, and ζ/L.

II1. Angular Corrections

Neglecting the solid-angle corrections, we have

$$\cos\theta=\cos\theta_{H_0}\cos\psi_0\left[1+\alpha\tan\theta_{H_0}+\beta\frac{\tan\psi_0}{\cos\theta_{H_0}}+\frac{\xi}{L_0}\sin\theta_{H_0}\cos\psi_0+\frac{\zeta}{L_0}\sin\psi_0\right] \quad \text{(II1.1)}$$

and for $\delta\theta=\theta_0-\theta$

$$\delta\theta=\cos\theta_0\left[\alpha\tan\theta_{H_0}+\beta\frac{\tan\psi_0}{\cos\theta_{H_0}}+\frac{\xi}{L_0}\sin\theta_{H_0}\cos\psi_0+\frac{\zeta}{L_0}\sin\psi_0\right]. \quad \text{(II1.2)}$$

Let us rewrite (II1.2) for convenience as

$$\delta\theta=C_\alpha\alpha+C_\beta\beta+C_\xi\xi+C_\zeta\zeta. \quad \text{(II1.3)}$$

TABLE VI. Symmetry.

Symmetry in	C_α	C_β	C_ξ	C_ζ
ψ_0	even	odd	even	odd
θ_{H_0}	odd	even	odd	even

Note the symmetries in the coefficients C. We indicate top, bottom, east, and west counter orientations by T, B, E, and W, respectively, and measure ξ positively east and ζ positively up. Taking note of the symmetry relations in Table VI, we have

$$\delta\theta_{TE}=C_\alpha\alpha+C_\beta\beta+C_\xi\xi/L_0+C_\zeta\zeta/L_0, \quad \text{(II1.4a)}$$

$$\delta\theta_{BE}=C_\alpha\alpha-C_\beta\beta+C_\xi\xi/L_0-C_\zeta\zeta/L_0, \quad \text{(II1.4b)}$$

$$\delta\theta_{TW}=-C_\alpha\alpha+C_\beta\beta-C_\xi\xi/L_0+C_\zeta\zeta/L_0, \quad \text{(II1.4c)}$$

$$\delta\theta_{BW}=-C_\alpha\alpha-C_\beta\beta-C_\xi\xi/L_0-C_\zeta\zeta/L_0. \quad \text{(II1.4d)}$$

We define a "top bottom" angular difference Δ_{TB} and an "east west" angular difference Δ_{EW}

$$\Delta_{TB}=\tfrac{1}{2}(\delta\theta_{TE}-\delta\theta_{BE})=\tfrac{1}{2}(\delta\theta_{TW}-\delta\theta_{BW}), \quad \text{(II1.5a)}$$

$$\Delta_{EW}=\tfrac{1}{2}(\delta\theta_{TE}-\delta\theta_{TW})=\tfrac{1}{2}(\delta\theta_{BE}-\delta\theta_{BW}). \quad \text{(II1.5b)}$$

We have three relationships among these quantities

$$\delta\theta_{TE}+\delta\theta_{BE}+\delta\theta_{TW}+\delta\theta_{BW}=0, \quad \text{(II1.6)}$$

$$\Delta_{TB}=C_\beta\beta+C_\zeta\zeta/L_0, \quad \text{(II1.7)}$$

$$\Delta_{EW}=C_\alpha\alpha+C_\xi\xi/L_0. \quad \text{(II1.8)}$$

II2. Solid-Angle Corrections

The first-order correction to L is

$$\delta L=\xi/L_0\sin\theta_{H_0}\cos\psi_0+\zeta/L_0\sin\psi_0, \quad \text{(II2.1)}$$

which yields to first order the solid-angle correction

$$\delta\Omega=2\xi/L_0\sin\theta_{H_0}\cos\psi_0+2\zeta/L_0\sin\psi_0. \quad \text{(II2.2)}$$

Following the nomenclature of Sec. II1,

$$\delta\Omega_{TE}=2\xi/L_0\sin\theta_{H_0}\cos\psi_0+2\zeta/L_0\sin\psi_0, \quad \text{(II2.3a)}$$

$$\delta\Omega_{TW}=2\xi/L_0\sin\theta_{H_0}\cos\psi_0+2\zeta/L_0\sin\psi_0, \quad \text{(II2.3b)}$$

$$\delta\Omega_{BE}=2\xi/L_0\sin\theta_{H_0}\cos\psi_0-2\zeta/L_0\sin\psi_0, \quad \text{(II2.3c)}$$

$$\delta\Omega_{BW}=2\xi/L_0\sin\theta_{H_0}\cos\psi_0-2\zeta/L_0\sin\psi_0. \quad \text{(II2.3d)}$$

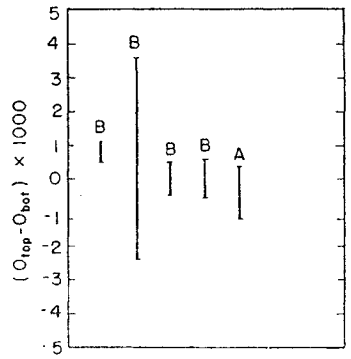

FIG. 29. The difference in the scale zeros 0_{Top}–0_{Bot} as determined in measurements A and B.

TABLE VII. Summary of measurements made to determine beam misalignment parameters.

Measurement	Description
A	Elastic scattering from a thin Au foil at angles near the zeros of the top and bottom scales.
B	Elastic and inelastic scattering from the 1.45-MeV state of Ni^{58} with the counters in the orientation TE, TW, BE, and BW at $\theta=15°$ and 30.5°.
C	Elastic scattering from Ni^{58} and Fe^{58} (data taking runs) in the orientation TE, BE, and exceptionally TW, BW (last runs).
D	Ozalid paper burn at the target position before the shift.
E	Ozalid paper burn at the target position after the shift.
F	Elastic scattering from Ni^{58} with the counters in the orientations TE, TW at $\theta=13.4°$ before the shift.

II3. Determination of Beam Misalignment Parameters

The three relations (II1.6), (II1.7), and (II1.8) establish the basis for determining the beam misalignment parameters α, β, ξ, and ζ. Table VII and Figs. 29, 30, and 31 list the measurements and show the graphical determination of these parameters. Table VIII summarizes the numerical values obtained for the parameters.

It was necessary to show that the zeros of both scales, 0_{Top} and 0_{Bot} lie in the same meridian plane. Measurements A and B in Table VII were made for this purpose. Measurement B utilizes Eq. (II1.6). Figure 29 shows the results obtained from measurement A and from measurement B. There are four points labeled B since two angles and two states (the ground state and the first excited state) were measured.

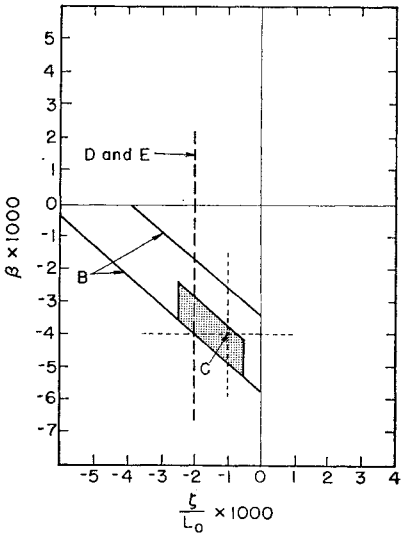

FIG. 30. The quantity β plotted versus ζ/L_0. The point C is determined from measurement C, the lines labeled B, D, and E are determined from measurements B, D, and E, respectively. The crosshatched area defines the allowed pairs of values that ζ/L_0 and β may take on when the uncertainties in the above measurements are taken into account.

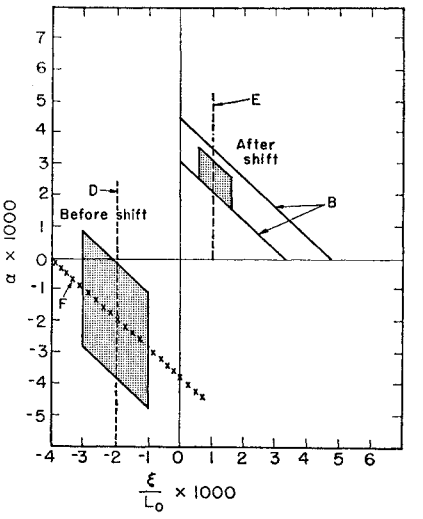

FIG. 31. The quantity α plotted versus ξ/L_0 before and after the shift. The lines labeled B, D, E, and F are determined from measurements B, D, E, and F, respectively. The crosshatched area defines the allowed pairs of values that ξ/L_0 and α may take on when the uncertainties in the above measurements are taken into account.

As described in Sec. C, the beam collimator system shifted position part way through the experiment. Consequently, the beam misalignment parameters had to be measured before and after the shift. It was found that there had been no vertical shift and that there had been a horizontal shift. Measurement C in conjunction with Eq. (II1.7) made it possible to determine a point in the $(\beta,\zeta/L_0)$ space. Measurement B determined the locus of points allowed, a straight line, and measurement D and E determine a line of constant ζ/L_0 in this space.

The horizontal parameter space $(\alpha,\xi/L_0)$ is shown in Fig. 31. Measurements F and B determine the locus of points allowed, a straight line; and measurements D and E determined lines of constant ξ/L_0 before and after the shift.

II4. Errors in Determination of Beam Misalignment Parameters

Uncertainties arise in the determination of the beam misalignment parameters which must be accounted for in order to estimate the systematic uncertainty for all

TABLE VIII. Summary of results obtained for beam misalignment parameters.

Parameter (units 10^{-3} radians)	Before shift	After shift
β	$-4\ \pm1$	$-4\ \pm1$
ζ/L_0	-1.5 ± 1	-1.5 ± 1
α	$-2\ \pm1$	$+2.5\pm0.8$
ξ/L_0	$-2\ \pm1$	$+1.1\pm0.5$

angular measurements. If $\Delta\alpha$, $\Delta\beta$, $\Delta\xi/L_0$, and $\Delta\zeta/L_0$ are the uncertainties in the beam misalignment parameters, the systematic angular uncertainty is $C_\alpha\Delta\alpha+C_\beta\Delta\beta+C_\xi\Delta\xi/L_0+C_\zeta\Delta\zeta/L_0$. Since the errors are independent, the systematic error is $\lambda_\alpha C_\alpha\Delta_\alpha+\lambda_\beta C_\beta\Delta\beta+\lambda_\xi C_\xi\Delta\xi/L_0+\lambda_\zeta C_\zeta\Delta\zeta/L_0$, where the four independent lambda parameters may vary between 0 and +1. Figure 32 shows the functions $f_i=C_i\Delta i$ (where $i=\alpha$, β, ξ/L_0, or ζ/L_0) and their sum for the case of maximum systematic uncertainties. The absolute values of f_i depend in a complicated fashion on a number of uncertainties in the measurement and are not discussed exhaustively here.

II5. Angular Corrections Due to Fluctuations in Beam Direction

When the monitors were located at $\pm15°$, where the elastic cross section changes rapidly with angle, the ratio of the monitor counting rates (mon$L$)/(mon$R$) can be used to determine fluctuation $\delta\Delta_{EW}(15°)$ in Δ_{EW} at 15° from run to run. Further, since $C_\xi=C_\alpha\cos\theta_0$ at small angles, the relation

$$\delta\Delta_{EW}(15°)=C_\alpha(15°)\delta\{\alpha+\xi/L_0\} \qquad \text{(II5.1)}$$

holds, and further the angular correction to the movable counter setting $\delta\Delta\theta$ is

$$[C_\alpha(\theta_0)/C_\alpha(15°)]\delta\Delta_{EW}(15°). \qquad \text{(II5.2)}$$

The monitors were not useful in the same way at the other settings (27° and 43.5° since these angles are near maxima in the elastic differential cross section. The relation

$$\delta\Delta\theta\leqq(\tan\theta_{H_0}/\tan\theta_0)(\delta\alpha+\delta\xi/L_0) \qquad \text{(II5.3)}$$

derived from Eq. (II1.2) was useful in determining the uncertainty in the angular correction. The uncertainties in α and ξ/L_0 due to fluctuations in the beam direction are denoted by $\delta\alpha$ and $\delta\xi/L_0$, respectively, in Eq. (II5.3).

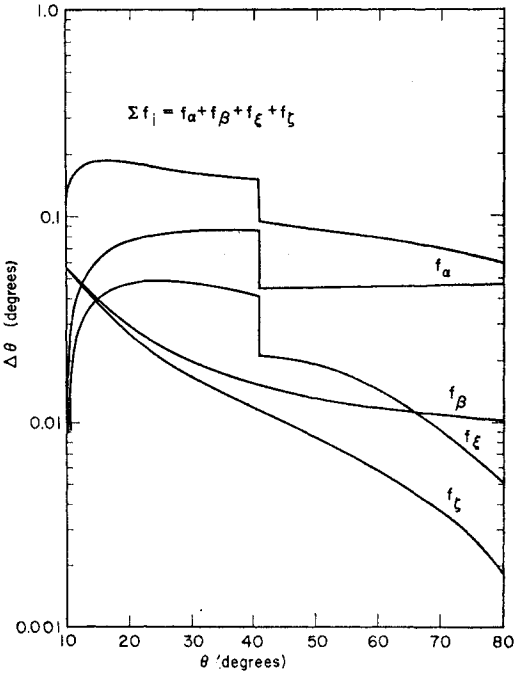

FIG. 32. The angular error quantities f_i plotted versus the laboratory scattering angle. The curve denoted Σf_i is the upper limit of the systematic error.

APPENDIX III: THE ANGULAR RESOLUTION FUNCTION FOR THE COUNTERS

III1. The Definition of the Angular Resolution Function

The counter collimator size and the beam spot size contribute about equally to the angular resolution function. The beam has a finite angular divergence.

We define the angular resolution function $N(\theta,\theta')$ such that

$$dn/n=N(\theta,\theta')d\theta', \qquad \text{(III1.1)}$$

where $n(\theta)$ is the number of particles detected at θ by the detector and $dn(\theta,\theta')$ is the number of particles arriving at the detector between θ' and $\theta'+d\theta'$. From Eq. (III1.1) it is obvious that

$$\int_{\theta_{min}'}^{\theta_{max}'}N(\theta,\theta')d\theta'=1. \qquad \text{(III1.2)}$$

III2. Angular Resolution Function for the Counter Collimator

The angular spreads due to a (a is parallel to the equatorial plane) and b are

$$\Delta_c\psi=b/L_0, \qquad \text{(III2.1a)}$$

$$\Delta_c\theta_H=a/L_0\cos\psi_0. \qquad \text{(III2.1b)}$$

By combining Eqs. (III2.1) and (II1.1) we obtain the resulting angular spread in θ,

$$\Delta_c\theta=\frac{\sin\theta_{H_0}\cos\psi_0}{\sin\theta_0}\Delta_c\theta_H+\frac{\sin\psi_0\cos\theta_{H_0}}{\sin\theta_0}\Delta_c\psi. \qquad \text{(III2.2)}$$

Lines of constant θ in the counter collimator are parallel, straight lines of slope $(-\tan\theta_{H_0}/\cot\psi_0)$. Depending on the sign of $(b/a-\tan\theta_{H_0}/\cot\psi_0)$, different configurations arise. The angular resolution function $N_c(\theta,\theta')$ is represented by a trapezoid centered at θ with bases $W+S$ and $W-S$ where the trapezoid parameters W and S are:

$$W=\max\left\{\begin{matrix}\sin\psi_0\cos\theta_{H_0}b/L_0\\(\sin\theta_{H_0}/\sin\theta_0)a/L_0\end{matrix}\right\}, \qquad \text{(III2.3a)}$$

$$S=\min\left\{\begin{matrix}\sin\psi_0\cos\theta_{H_0}b/L_0\\(\sin\theta_{H_0}/\sin\theta_0)a/L_0\end{matrix}\right\}. \qquad \text{(III2.3b)}$$

III3. Angular Resolution Function for Beam Size and Beam Angular Divergence

An investigation similar to that described in Sec. III2 shows the angular resolution function dependent on the beam characteristics $N_B(\theta_0,\theta')$ is represented by a trapezoid centered at θ with bases $W+S$ and $W-S$ where

$$W=\max\left\{\begin{array}{l}\left(\Delta_B\beta+\dfrac{\Delta_B\zeta}{L_0}\cos\theta_0\right)\dfrac{\sin\psi_0}{\sin\theta_0}\\ \left(\Delta_B\alpha+\dfrac{\Delta_B\xi}{L_0}\cos\theta_0\right)\dfrac{\sin\theta_{H_0}\cos\psi_0}{\sin\theta_0}\end{array}\right\},$$

$$S=\min\left\{\begin{array}{l}\left(\Delta_B\beta+\dfrac{\Delta_B\zeta}{L_0}\cos\theta_0\right)\dfrac{\sin\psi_0}{\sin\theta_0}\\ \left(\Delta_B\alpha+\dfrac{\Delta_B\xi}{L_0}\cos\theta_0\right)\dfrac{\sin\theta_{H_0}\cos\psi_0}{\sin\theta_0}\end{array}\right\}.$$

III4. Convolution of Beam and Collimator Angular Resolution Functions

To account for both collimator size and beam size and angular divergence, we must perform the integration

$$N(\theta_0,\theta')=\int_{\theta\min}^{\theta\max}N_B(\theta_0,\theta)N_C(\theta,\theta')d\theta. \quad \text{(III4.1)}$$

Since N_B and N_C are trapezoids, N is a curve composed of arcs of parabolas and of straight lines. This may be approximated to sufficient accuracy by a trapezoid whose upper (smaller) base is

$$|W_B-W_C|-(S_B+S_C) \quad \text{(III4.2)}$$

unless this quantity is negative. If negative, the upper base is zero. The lower base is

$$W_B+W_C+S_B+S_C. \quad \text{(III4.3)}$$

A width W is defined by a rectangle having the same area and height to complete the specification of $N(\theta_0,\theta')$.

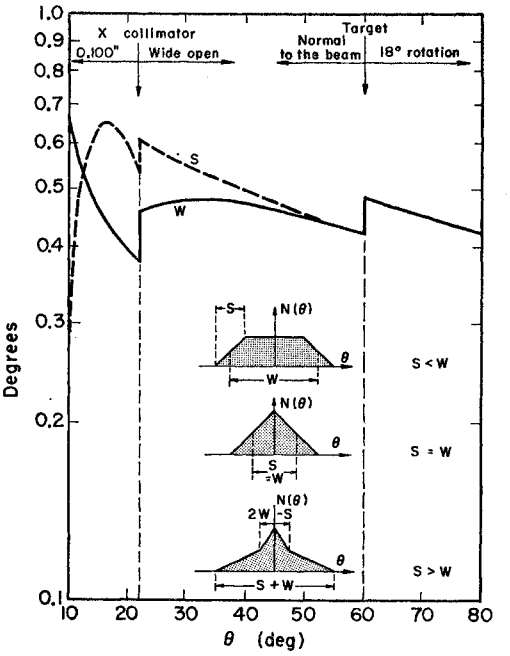

FIG. 33. The trapezoid parameters W and S which determine the angular resolution function are plotted against scattering angle θ. The angular resolution function is a convolution of collimator-size and beam-size resolution functions. At the top of the graph, the settings for the X collimator and the target orientation are noted. Characteristic shapes of the resolution function are shown for S less than, equal to, and greater than W.

One can show

$$W=\left[\int_{-\pi}^{\pi}N_B(\theta_0,\theta)N_C(\theta_0,\theta)d\theta\right]^{-1}. \quad \text{(III4.4)}$$

These three quantities have been summarized in Fig. 33, and simplified shapes for the angular resolution functions are also shown.

For the runs where the target has been rotated ($\theta>60°$) a correction has been added to W corresponding to an increase in the width of the angular resolution function of $\Delta_B\xi/L_0\tan\omega\sin\theta_0$, where ω is the angle the plane of the target surface makes with the target plane.

APPENDIX IV: CORRECTIONS AND UNCERTAINTIES

In this Appendix all corrections and uncertainties greater than 0.1% are tabulated as Tables IX–XIII.

TABLE IX. Absolute cross sections: uncertainties.

Quantity	Origin of uncertainty	Magnitude of uncertainty
Collimator areas	Measurement uncertainty	±0.5%
Target-collimator distance	(a) collimator thickness	±0.25%
	(b) measurement uncertainty	±0.05% } ±0.29%
Absolute counter efficiency	Assumed to be 100%	Two counters equally efficient within ±0.4%
Target thickness	(a) uncertainty in area of sample	Ni^{58} ±1% Fe^{58} ±1%
	(b) uncertainty in weight of sample	±0.17% ±0.17%
	(c) inhomogeneity of target	±2% } ±2.24% ±2.5% } ±2.70%
Beam current	Reproducibility of calibrations	±0.3%
Others	Statistics, analysis, fit	Ni^{58} ±0.46% Fe^{58} ±0.47%

TABLE X. Absolute cross sections: corrections and uncertainties in them.

Correction	Magnitude	Uncertainty
Weight of contaminants in target	Ni^{58}: 0.36% Fe^{58}: 1.05%	±0.05% ±0.06%
Corrections to solid angle due to beam misalignment	0.11%	±0.14%
Discrepancy between internal and external Faraday cups	1%	±1.3%
Total uncertainty in absolute cross sections		Ni^{58}: ±2.7% Fe^{58}: ±3.1%

TABLE XI. Relative cross sections: uncertainties.

Uncertainty	Origin of uncertainty	Magnitude
Counter statistics Monitor statistics		Varies
Analysis uncertainty	Peak shape	Varies
Relative normalization of the monitor settings	Statistics, fit	≈±0.8% for various normalizations
Normalization of the monitor for $\theta_{c.m.}>56°$	Statistics, fit	±2.2%
Possible systematic error for $\theta_{c.m.}>56°$	Conservative estimate of error based on fluctuation of the single monitor counter relative to the Faraday cup	Ni^{58}: ±2% Fe^{58}: ±1.7%

TABLE XII. Relative cross sections: corrections and uncertainties in them.

Correction	Magnitude	Uncertainty
Relative normalization of the two movable counters:		
solid-angle ratio	3.95%	±0.3%
second-order corrections to solid angle ratio	0.10%	±0.07%
relative efficiencies of the two counters	Assumed equal	Verified within ±0.4%
Pulse-height analyzer nonlinearity	0–3% (gs) 0–5% (fe)	0–±2%
Subtraction of light contaminants		
Nickel gs $15°<\theta_{c.m.}<20°$	<1.5%	±10% of correction
Nickel fe $15°<\theta_{c.m.}<23.5°$	<24%	
Iron gs $14°<\theta_{c.m.}<20°$	<3.5%	±40% of correction
Iron fe $\theta_{c.m.}<20°$	<14%	
Subtraction of heavy contaminants	Ni^{58} gs 1% fe 0.5%	±2% ±1%
$\theta_{c.m.}>56°$	Fe^{58} gs and fe 1%	±1%

TABLE XIII. Angular corrections and uncertainties.

Quantity	Origin of correction or uncertainty	Correction	Uncertainty
Absolute angle	Beam misalignment	≦0.2°	≦0.2° (see Appendix II, Fig. 32)
Angular acceptance	Finite geometry: angular acceptance ≈0.5° (see Appendix III, Fig. 33)	not unfolded	
Relative angles	Uncertainty in scale angle due to television (±0.05°)	none	0 to ±0.05°
	Horizontal fluctuations of beam		
	$\theta_{c.m.}<15°$	0 to 0.08°	0 to 0.02°
	$\theta_{c.m.}>15°$	not made	±0.08
	Vertical fluctuations of beam	believed negligible	